nature photonics

Article https://doi.org/10.1038/s41566-023-01242-9

High-bandwidth perovskite photonic sources on silicon

In the format provided by the authors and unedited

Contents

Supplementary Notes 1-7 2

Supplementary Note 1. Charge carrier dynamics and modulation characteristics 2

Supplementary Note 2. Elliott modelling 3

Supplementary Note 3. Temperature dependence of photoluminescence 4

Supplementary Note 4. Time-resolved photoluminescence measurement 4

Supplementary Note 5. Transient absorption spectroscopy 5

Supplementary Note 6. Optical pump Terahertz probe spectroscopy 5

Supplementary Note 7. External quantum efficiency measurement 9

Supplementary Figures 1-38 11

References 49

Supplementary Notes 1-7

Supplementary Note 1. Charge carrier dynamics and modulation characteristics

- **Carrier density estimation**

The effective carrier lifetime (τ_{eff}) of a perovskite emitter is given by the derivative of the recombination rates with respect to carrier density,

$$\tau_{eff}{}^{-1} = k_1 + 2k_2 n + 3k_3 n^2. \quad (1)$$

The τ_{eff} is related to the achievable -3 dB bandwidth (f_{-3dB}) as,

$$\tau_{eff}{}^{-1} = 2\pi f_{-3dB}. \quad (2)$$

Based on the equations, we can determine the intrinsic modulation bandwidth of the emitter, which only depends on the τ_{eff} rather than the resistance-capacitance (RC) related time constant (τ_{RC}).

The device carrier density corresponding to a given current I can be estimated by the following integral[1],

$$n\ I\ = \frac{\eta_{inj}}{eAd}\int_0^I \tau_{eff} dI, \quad (3)$$

where η_{inj} is the injection efficiency, e is the elementary charge, A is the device active area, d is the thickness of the emitter. The η_{inj} can be estimated from the external quantum efficiency (EQE), photoluminescence quantum efficiency (PLQE) of the emitter, and outcoupling efficiency η_{out},

$$EQE\ = \eta_{inj} \times PLQE \times \eta_{out}. \quad (4)$$

- **Theoretical RC-limited modulation bandwidth estimation**

The equivalent circuit of a perovskite LED can be simplified as a diode resistor (R_d), a capacitor (C), and a series resistor (R_s). At a low modulation frequency, the capacitor can be regarded as an open circuit. At a relatively high modulation frequency, the value of C tends to its intrinsic capacitance (as a parallel-plate capacitor) while the trap-related capacitance can be ignored (Extended Data Fig. 8). The sum of R_d and R_s can be estimated as the differential resistance (Supplementary Fig. 29).

Supplementary Note 2. Elliott modelling

- **Extracting exciton properties from absorption spectra analysis**

To extract the exciton binding energy (E_b), we fit the absorption spectra to include both the lowest energy $1s$ excitonic transition states (α_b) and unbound continuum absorption states (α_c) based on the Elliott model,

$$\begin{aligned}\alpha\ \hbar\omega\ &= A\cdot\Theta(\hbar\omega-E_g)\cdot D_{CV}\cdot\left(\frac{\pi e^{\pi x}}{\sinh \pi x}\right)+A\cdot E_b\sum_{n=1}^{\infty}\frac{4\pi}{n^3}\delta\left(\hbar\omega-E_g+\frac{E_b}{n^2}\right)\\ &\propto \frac{\mu_{CV}^2}{\hbar\omega}\left[4\pi\sqrt{E_b^3}\,\mathrm{sech}\left(\frac{\hbar\omega-E_g+E_b}{\Gamma}\right)+\int_{E_g}^{\infty}\mathrm{sech}\left(\frac{\hbar\omega-E}{\Gamma}\right)\frac{2\pi\sqrt{E_b}}{1-e^{-2\pi\sqrt{\frac{E_b}{E-E_g}}}}dE\right],\end{aligned} \tag{5}$$

where μ_{CV}^2 is the squared transition dipole moment, E_g is the bandgap, E_b is the exciton binding energy. The first term is related to the exciton-related absorption, and the second term is the contribution from the continuum states. A hyperbolic secant function is used to simulate the line broadening and the non-parabolic dispersion of energy band. A Gaussian function is convoluted with the delta function and the Heaviside step function, respectively. The line width is described by Γ.

Supplementary Note 3. Temperature dependence of photoluminescence

- **Determination of electron-phonon coupling strength**

The electron–phonon coupling in the perovskites can be ascribed to the Fröhlich interaction between the longitudinal optical (LO) mode phonons and electrons. The full width at half-maximum (FWHM) of the photoluminescence (PL) spectra on temperature can be expressed as,

$$\Gamma\ T\ = \Gamma_0 + \Gamma_{LO} = \Gamma_0 + \gamma_{LO} \cdot \frac{1}{e^{E_{LO}/k_B T} - 1}, \quad (6)$$

where Γ_0 is the temperature-independent inhomogeneous broadening term caused by scattering due to disorder and imperfections, Γ_{LO} is the homogeneous broadening terms result from the LO phonon (Fröhlich) scattering, γ_{LO} is the electron-phonon coupling strength, and E_{LO} is the LO phonon energy. These parameters can be extracted by using the Gauss-fitted results of the FWHM of the PL spectra as a function of temperature.

Supplementary Note 4. Time-resolved photoluminescence measurement

- **Initial carrier density calculations**

Initial carrier density n_0 of the perovskite films in the time-resolved photoluminescence (TRPL) measurements can be estimated by,

$$n_0 = \frac{\alpha \cdot P}{E_{ph} \cdot f} \times \frac{1}{\pi (s/2)^2 \cdot d}, \quad (7)$$

where α is the absorption of the film, s is the FWHM of the Gaussian beam diameter, P is the laser power, f is the laser repetition rate, E_{ph} is the photon energy ($E_{ph} = \hbar\omega$), and d is the film thickness[2].

Supplementary Note 5. Transient absorption spectroscopy

- **Initial carrier density calculations**

The number of photons absorbed (per pulse) = fluence (per pulse)$\times(1-10^{-OD})/h\nu$, where OD is the optical density of the material measured by UV-Vis spectroscopy, h is the Planck constant, ν is the frequency of light. Fluence per pulse can be calculated by fluence (per pulse) = $P/(f\times S)$, where P is the pump power measured by a power meter, f = 500 Hz is the repetition rate of the Transient absorption (TA) system, $S = \pi r^2$ is the area of the pump beam spot (r: beam spot radius measured by a beam profiler, THORLABS BC106N-VIS/M, 350 – 1100 nm). In this work, the effective beam diameter is $2\times r$ = 1600 μm for all TA measurements. Film thicknesses of 84.9 nm (control), 110.6 nm (MA), 83.8 nm (PEA) and 91.8 nm (*t*-BA) were used to calculate the absorbed photon density.

The normalised TA kinetics $\Delta A(t)$ were multiplied with the initial charge carrier density n_0, taking the time derivative of this carrier density $n(t)$,

$$n(t) = n_0 \times \Delta A(t). \tag{8}$$

Taking the time derivative of the carrier density $n(t)$, the curves of $-dn(t)/dt$ as a function of $n(t)$ can be plotted[2].

Supplementary Note 6. Optical pump Terahertz probe spectroscopy

- **Determination of photoconductivity**

The THz pulse transmitted through a sample is altered by the photo-induced change in the permittivity of the sample (assuming the substrate permittivity is not affected by photoexcitation), so the transmitted THz pulses with and without optical excitation of the sample are measured and compared. Under certain limits and approximations there is a simple expression for the (complex) fractional change in the transmitted wave – the ratio of the

difference between the waves transmitted with and without optical excitation $\Delta E(= E_{on} - E_{off})$, to the wave transmitted without optical excitation E_{off}[2]. The expression considers a layer that is uniformly photoexcited throughout its depth and the two layers either side adjacent to the perovskite layer that are not photoexcited. In this work the sample layers are thinner than one absorption depth, so it is approximated that they are uniformly excited throughout their thickness. The limits that simplify the expression are that the photoexcited layer (the sample) is thin while the substrate is thick compared to the THz pulse length (on the order of the THz wavelength), and that the photoexcited layer (the sample) is optically thin at THz frequencies ($n\omega d/c \ll 1$, where n is the complex refractive index of the photoexcited layer, c is the speed of light, d is the thickness of photoexcited layer, and ω is the THz frequency). Then the complex fractional change in transmission is found to be proportional to the change in permittivity of the sample layer:

$$\epsilon_s^* \ \omega \ - \epsilon_s \ \omega \ = \ -\frac{ic(n_1(\omega)+n_2(\omega))}{\omega d}\frac{\Delta E(\omega)}{E_{off}(\omega)}, \tag{9}$$

where n_1 is the complex refractive index of the layer before the photoexcited layer (nitrogen, $n_1 = 1$), n_2 is the complex refractive index of the layer after the photoexcited layer (quartz, $n_2 = 2.092$)[3], ϵ_s is the complex permittivity of the sample, and * indicates photoexcited.

The permittivity has contributions from free and bound charges:

$$\epsilon \ \omega \ = \epsilon_L \ \omega \ + \frac{i\sigma(\omega)}{\omega\epsilon_0}, \tag{10}$$

where ϵ_L is the complex permittivity of the lattice (bound charges), σ is the complex conductivity and ϵ_0 is the permittivity of vacuum. If the change is dominated by the change in the free charge contribution i.e., the conductivity, the fractional change in the transmitted wave can be wholly attributed to the change in conductivity:

$$\Delta\sigma \ \omega \ = \ -\frac{(n_1(\omega)+ n_2(\omega))}{Z_0 d}\frac{\Delta E(\omega)}{E(\omega)}, \tag{11}$$

where Z_0 is the vacuum impedance.

Photoexcitation changes the conductivity by generating additional free carriers Δn (whose mobility, μ, may actually vary as a function of their position in the bands), as the conductivity

is proportional to the product of the free carrier density and the mobility. This photo-induced change in conductivity (photoconductivity) is the sum of the photoexcited electron and hole contributions, $\Delta\sigma\ t\ = e\big(\Delta n_e(t)\mu_e\ t\ +\ \Delta n_h(t)\mu_h\ t\ \big)$, and immediately after photoexcitation (t=0) the densities of photoexcited electrons and holes are equal:

$$\Delta\sigma\ 0\ = e\Delta n_e(0)(\mu_e\ 0\ + \mu_h\ 0\ , \tag{12}$$

where subscripts e and h indicate electrons and holes respectively. Therefore, if the initial electron and hole densities can be estimated from the absorption of the incident photon density, then the initial value of $\Delta E/E$ can be used to find the initial sum mobility (electron mobility plus hole mobility).

For photoconductivity decay measurements, the relative delay of the THz generation and detection beams is fixed such that the peak of the temporal waveform of the THz pulse is measured, and then the delay between the optical pump and this THz probe is varied. As the pump-probe delay time varies, the photoconductivity changes, and this change is assumed to be dominated by the change in electron and hole density due to recombination processes rather than changes in their mobility. Therefore, the photoconductivity decay can be fit with rate equations.

- **Initial carrier densities and effective charge-carrier mobility calculations**

The incident pump fluence is the energy per pump pulse per area, which is calculated using the averaged pump power, the pump pulse repetition rate and the pump area on the sample. The pump profile is approximated as a Gaussian, so the fluence distribution is given by:

$$F\ r\ = F_0\ e^{\frac{-r^2}{2\sigma^2}} = \frac{E_{pump}}{2\pi\sigma^2}\ e^{\frac{-r^2}{2\sigma^2}}, \tag{13}$$

where the amplitude F_0 is such that the integral of this fluence distribution over the area gives the total energy per pump pulse, E_{pump}(and σ is the standard deviation of the pump beam's Gaussian profile). The spatial distribution of photons per pulse is then found by dividing this fluence by the energy per photon at this pump wavelength, E_{photon}. The fraction of the incident photons absorbed is given by $f = (1 - R - T)$ where R and T are the fractions of the incident

light intensity that are reflected and transmitted, respectively. An unknown fraction of these absorbed photons may generate free carriers that absorb THz radiation, called the free carrier yield, φ. The expression for photoexcited free carriers per area is:

$$\Delta n\ r\ =\ \Delta n_0\ e^{\frac{-r^2}{2\sigma^2}} =\ \varphi(1-R-T)\frac{E_{pump}}{E_{photon}2\pi\sigma^2}\ e^{\frac{-r^2}{2\sigma^2}}, \tag{14}$$

where Δn_0 is the carrier number per area at the peak of Gaussian profile. This expression is used to calculate the absorbed photons per area, $\Delta n_0'$, which omits the unknown free carrier yield $\boldsymbol{\varphi}$ (so $\Delta n_0 = \varphi\ \Delta n_0'$).

The measured quantity $\Delta E/E_{off}$ is proportional to the carrier density, which has a non-uniform transverse profile (Gaussian), and the total signal is proportional to a summation (integral) of the carrier density over the area of the probe. Since the probe has a non-uniform transverse profile (Gaussian), the integral of the carrier density over the probe area is weighted by the transverse profile of the field strength of the THz probe. Assuming the Gaussian profiles are centred on the same position, this gives the average carrier number per area that is probed as:

$$\langle\Delta n\rangle =\ \Delta n_0\ \frac{\sigma_{pump}^2}{\sigma_{pump}^2+\ \sigma_{THz}^2}. \tag{15}$$

This initial average number absorbed per area (excludes the unknown free carrier yield φ), $\langle\Delta n'\rangle$, is inserted into one of the two expressions for photoconductivity, (11) and (12), which are equated (12) so that they can be rearranged to give the initial effective sum mobility, $\varphi\sum\mu$.

$$\Delta\sigma\ \omega\ =\ -\frac{n_1+\ n_2}{Z_0 d}\frac{\Delta E\ \omega}{E\ \omega} = \frac{\langle\Delta n'\rangle e\varphi\sum\mu(\omega)}{d}. \tag{16}$$

Since the expression (11) is derived assuming that the carrier density is uniform through the thickness of the film, the volume density in (12) is found by dividing the area density by the thickness of photoexcited layer, *d*.

- **Charge carrier diffusion length calculations**

The charge carrier diffusion length as a function of carrier density *n* can be calculated from decay rates and mobilities[4],

$$L\ n\ =\ \sqrt{\frac{D}{R_{total}(n)}} =\ \sqrt{\frac{\mu k_B T}{eR_{total}(n)}}, \tag{17}$$

where $D = \mu k_B T e^{-1}$ is the diffusion constant at room temperature T, which can be determined from the carrier mobility μ and the total charge carrier recombination rate $R_{total}\ n$. $R_{total}\ n$ can be derived from the rate constants (in the main text) as follows,

$$R_{total}\ n = -\frac{1}{n}\frac{dn}{dt} = \varphi^2 k_3 \left(\frac{n}{\varphi}\right)^2 + \varphi k_2 (n/\varphi) + k_1. \tag{18}$$

Supplementary Note 7. External quantum efficiency measurement

- **External quantum efficiency calculations**

In this work, the EQE of a device was measured by aligning the device and an optical power head in a collimated bracket. The device was driven by a sourcemeter as the voltage/current source. The optical power head was placed in front of the device with a fixed distance d of 10 cm to measure the emitted light from the forward perpendicular direction[5]. The effective solid angle subtended by the optical power head Ω_P can be described as

$$\Omega_P = 2\pi\left(1 - cos\frac{r_P}{d}\right), \tag{19}$$

where r_P is the effective active area of the optical power head, d is the distance between the device and power head.

The average emitted photon energy E_{avg} (eV Photon^{-1}) can be derived from the electroluminescence (EL) emission spectrum, defined as

$$E_{avg} = \frac{\int \varphi_{EL}\ \lambda\ \frac{hc}{\lambda} d\lambda}{\int \varphi_{EL}\ \lambda\ d\lambda}, \tag{20}$$

where $\varphi_{EL}\ \lambda$ is the EL intensity (a.u.) at the wavelength of λ, h is the Planck's constant, c is the speed of light.

The radiant intensity $I_{radiant\ intensity}$ (W sr^{-1}) denotes the power emitted, reflected, transmitted or received by a surface per unit solid angle $d\Omega$, which can be described as

$$I_{radiant\ intensity} = \frac{P}{\Omega_P} = \Phi_P E_{avg}, \tag{21}$$

where P is the measured power value of the optical power head (has been corrected by its quantum efficiency), Φ_P is the photon flux (photon sr^{-1} s^{-1}) at the same surface area of the optical power head.

The photon flux over the whole forward hemisphere Φ (photon sr^{-1} s^{-1}) can be described as

$$\Phi = \frac{1}{E_{avg}} \int_0^{2\pi} d\varphi \int_0^{\pi/2} I_{radiant\ intensity}\ \theta\ sin\theta\, d\theta$$

$$= \int_0^{\pi/2} 2\pi \Phi_P\ \theta\ cos\theta sin\theta\, d\theta, \tag{22}$$

where φ is the azimuthal angle and θ is the polar angle. Note that Lambertian assumption is invalid in this work. The $I_{radiant\ intensity}$ and $\Phi_P\ \theta$ depend on the EL profile, and can be determined by $P\ \theta$ $(I_{radiant\ intensity\ \theta} = \frac{P\ \theta}{\Omega_P} = \Phi_P\ \theta\ E_{avg})$.

Hence, the EQE of the device can be obtained by

$$EQE = \frac{\Phi}{I/q} = \frac{2\pi q \int_0^{\pi/2} P\ \theta\ cos\theta sin\theta d\theta}{\Omega_P E_{avg} I}, \tag{23}$$

where I is the measured current of the device, q is the elementary charge.

Supplementary Figures 1-38

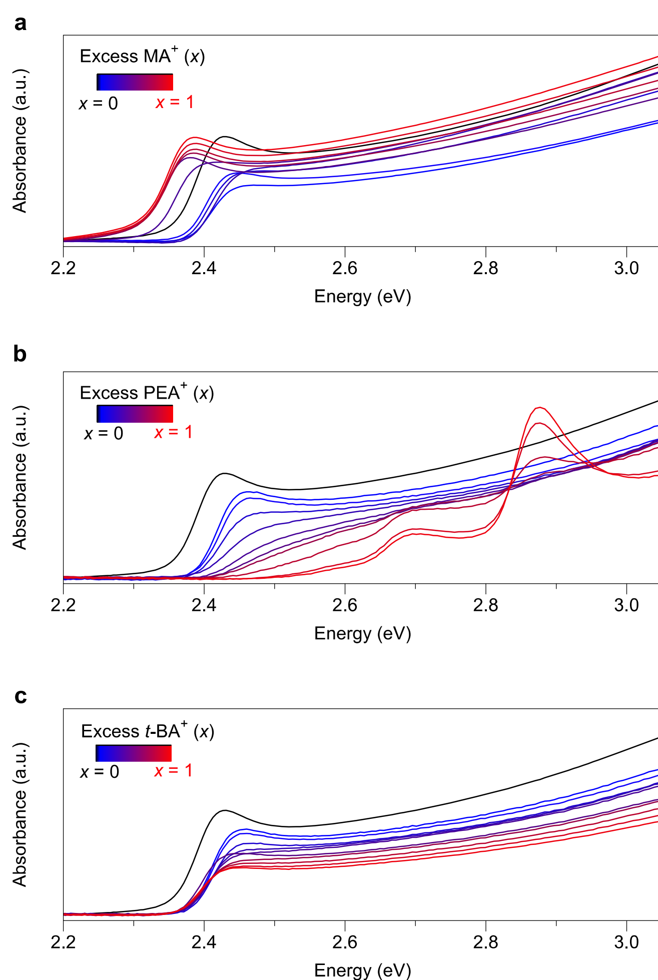

Supplementary Fig. 1 | Absorption characteristics of the perovskite films versus the molar excess of the alkylammonium cations. Ultraviolet–visible absorbance spectra of the MA^+ (**a**), PEA^+ (**b**), and *t*-BA^+ (**c**) modified films with the molar excess varied from 0 to 1 with respect to $PbBr_2$.

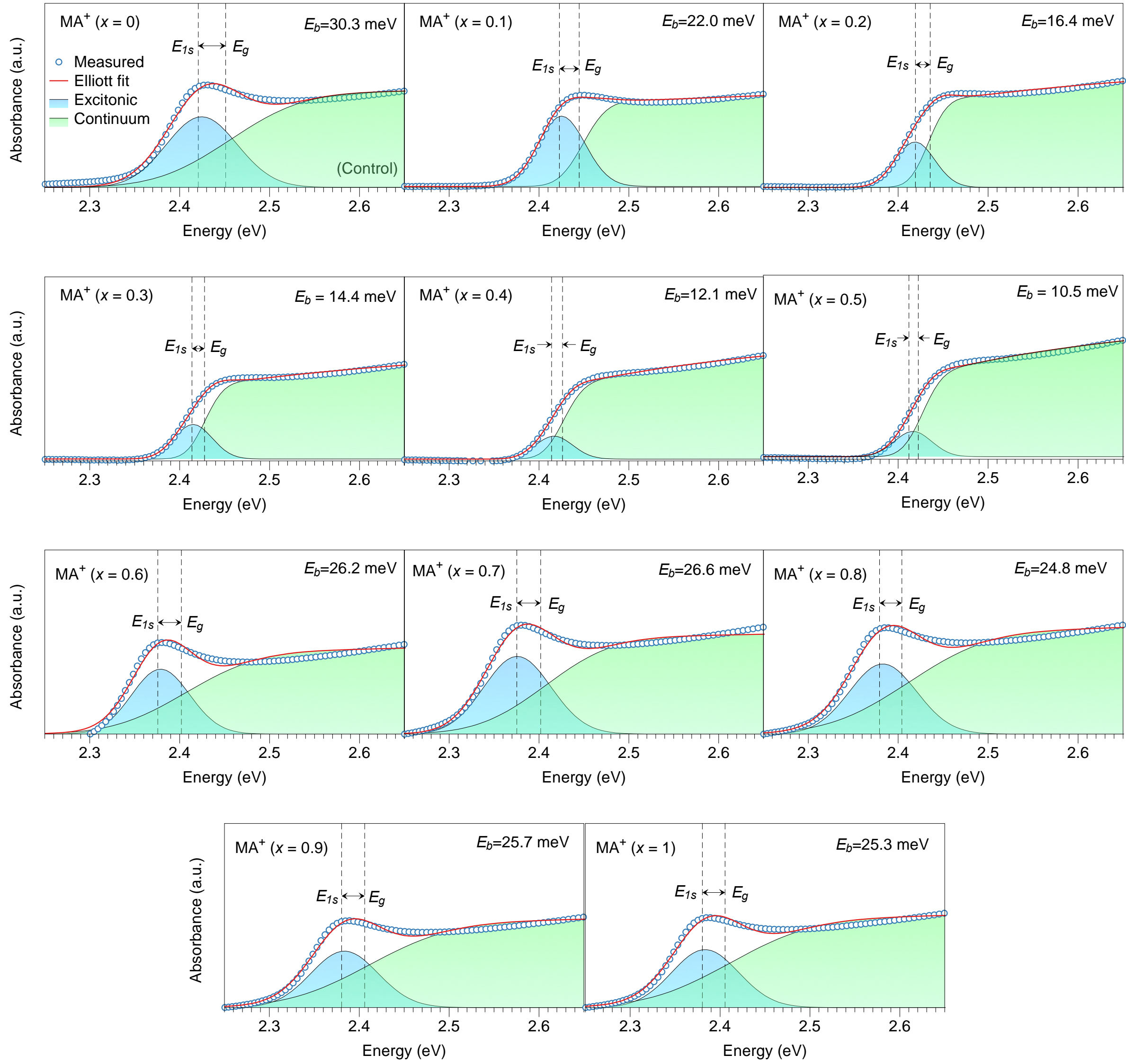

Supplementary Fig. 2 | Exciton binding energies of the MA-modified films. Elliott's theory for absorption onset modelling of the MA^+ modified films with the molar excess varied from 0 to 1 with respect to $PbBr_2$. The measured absorption spectra (blue open circles) are fitted according to the Elliott formula (red lines) with the contribution from the excitonic and continuum band transitions.

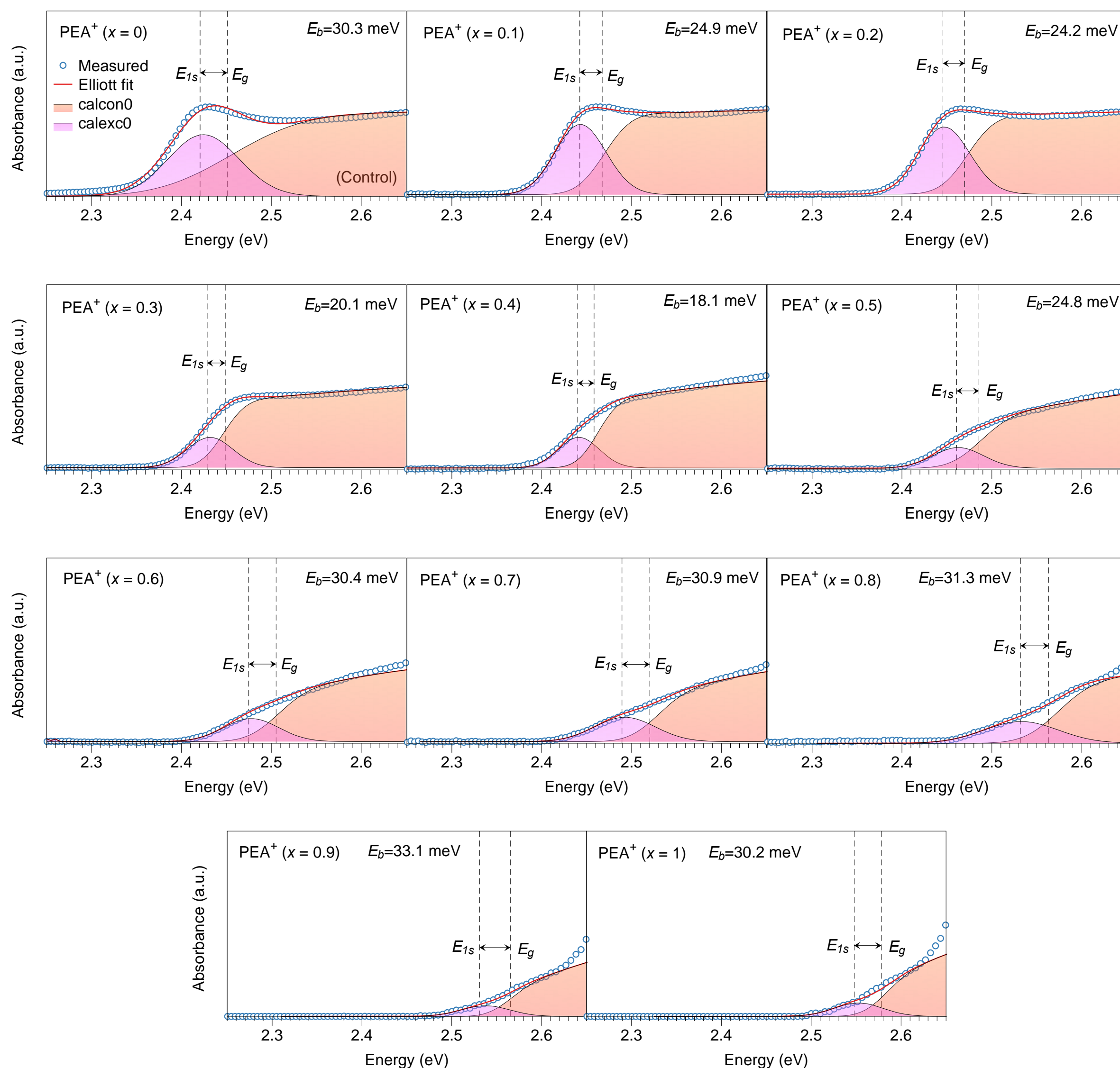

Supplementary Fig. 3 | Exciton binding energies of the PEA-modified films. Elliott's theory for absorption onset modelling of the PEA^+ modified films with the molar excess varied from 0 to 1 with respect to $PbBr_2$. The measured absorption spectra (blue open circles) are computed according to the Elliott formula (red lines) with the contribution from the excitonic and continuum band transitions.

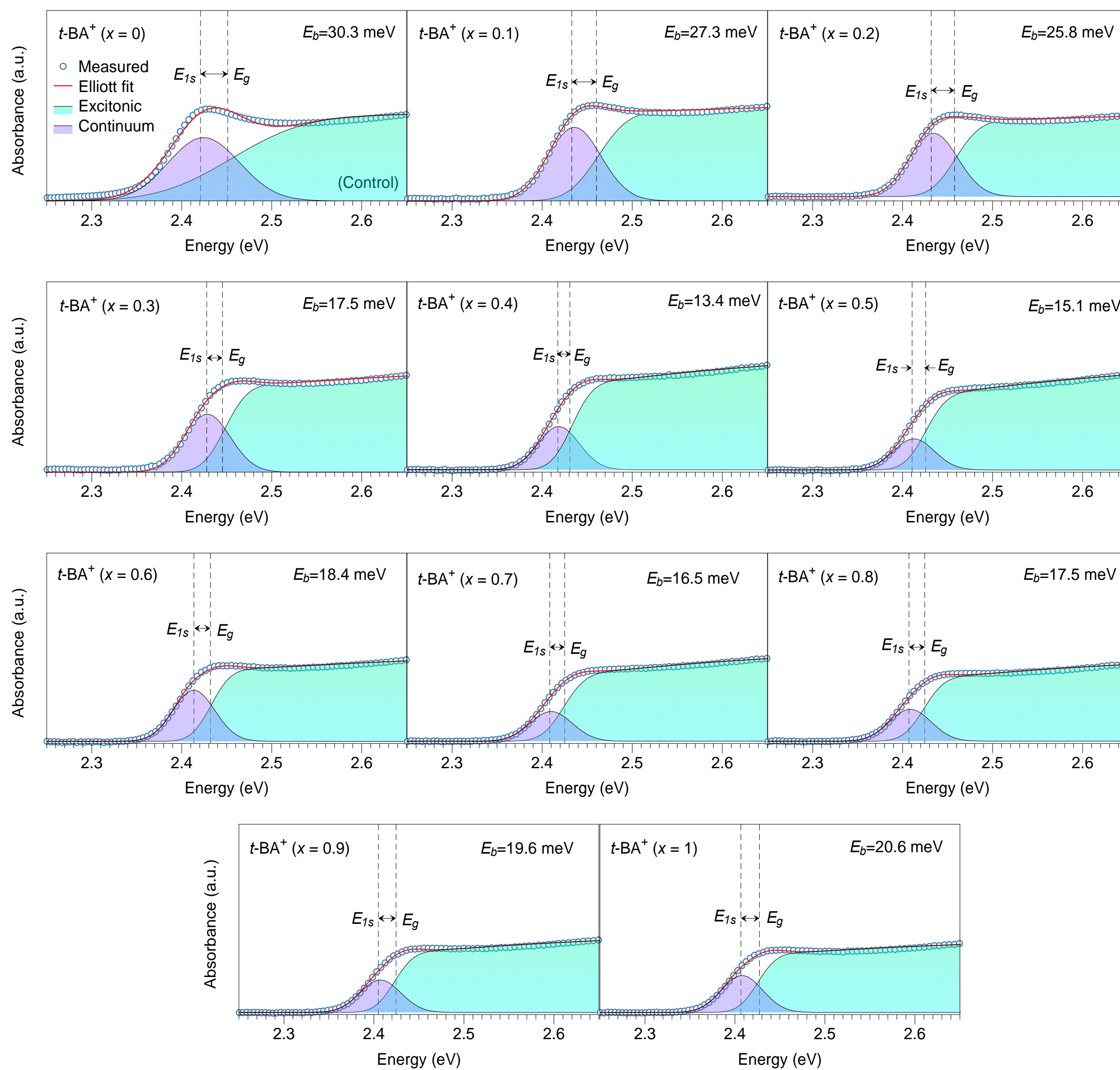

Supplementary Fig. 4 | Exciton binding energies of the *t*-BA-modified films. Elliott's theory for absorption onset modelling of the *t*-BA^+ modified films with the molar excess varied from 0 to 1 with respect to $PbBr_2$. The measured absorption spectra (blue open circles) are computed according to the Elliott formula (red lines) with the contribution from the excitonic and continuum band transitions.

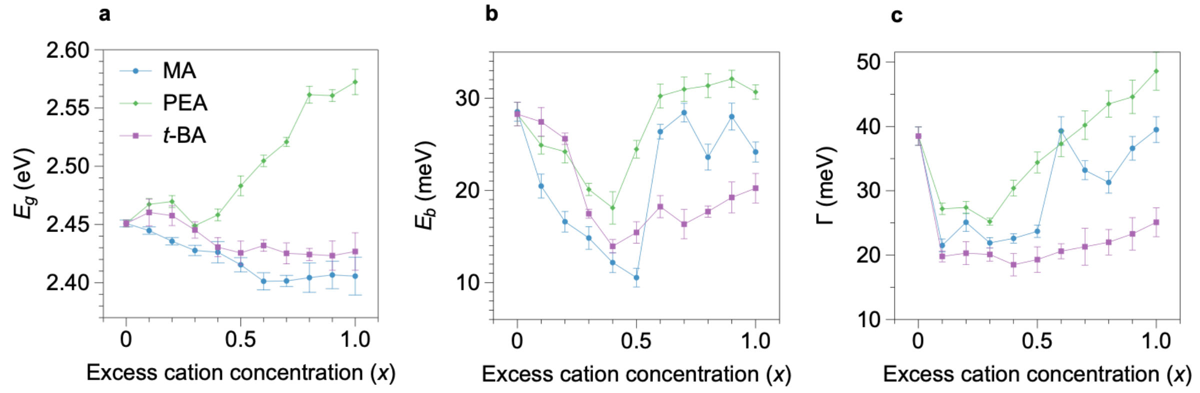

Supplementary Fig. 5 | Changes in exciton binding energy, band gap and broadening parameter of the perovskite films. a-c, Calculated band gap E_g (**a**), exciton binding energy E_b (**b**) and broadening parameter Γ (**c**) of the perovskite films varying the molar excess of the alkylammonium cations. Error bars indicate standard error of mean of 5 independent fittings.

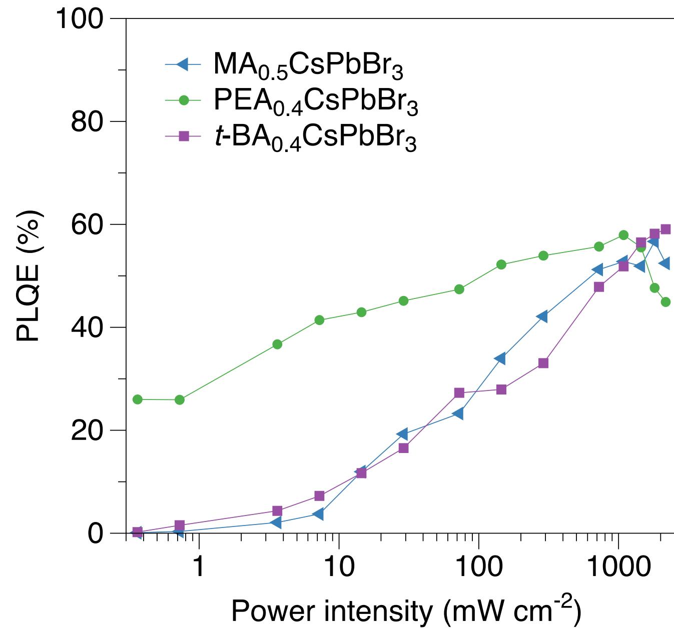

Supplementary Fig. 6 | PLQE characteristics of the optimal perovskite films. PLQE line plots of the optimal compositions as a function of the continues-wave pumped power intensity.

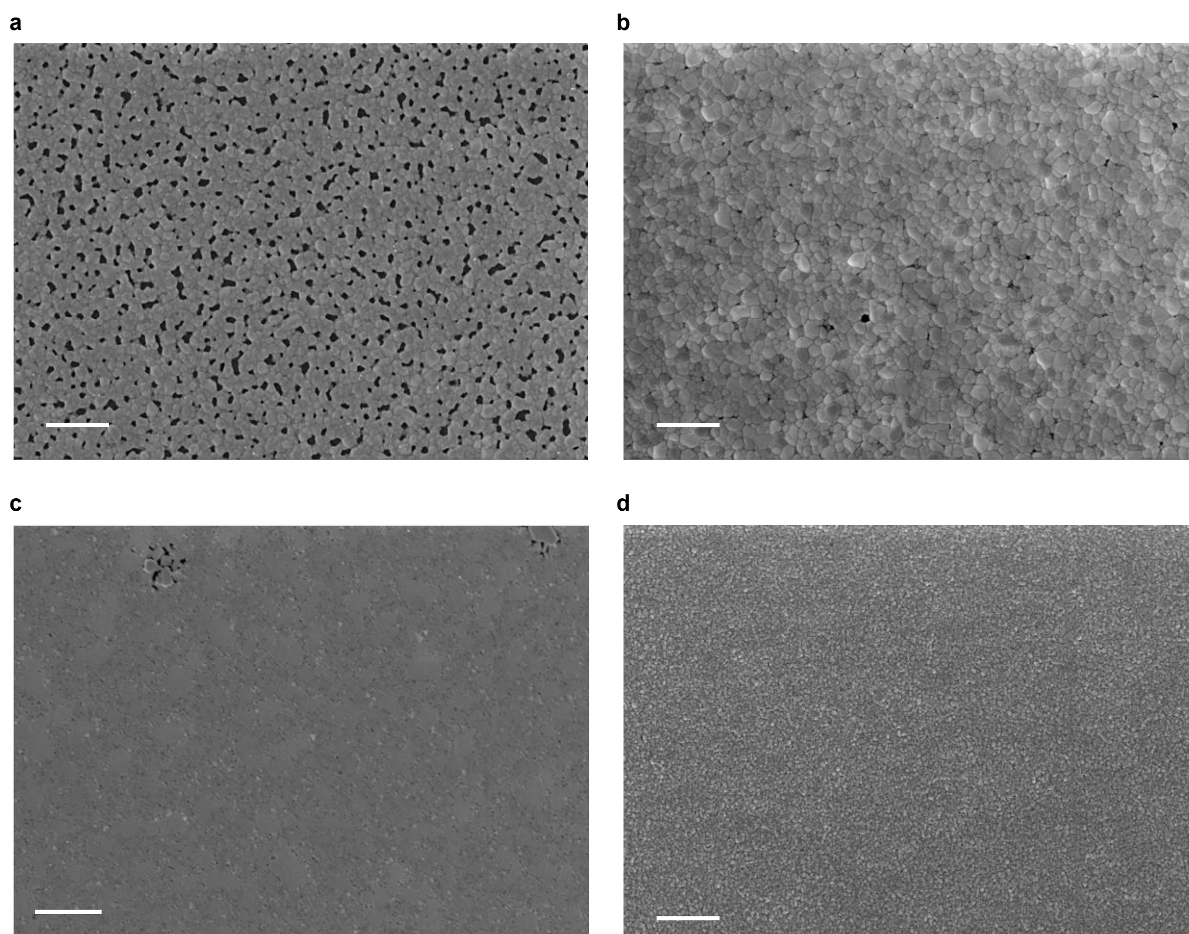

Supplementary Fig. 7 | Surface morphology of the alkylammonium cation-modified perovskite films. a-d, Secondary electrons scanning electron microscopy (SEM) images of the control (**a**), MA (**b**), PEA (**c**) and *t*-BA (**d**) films deposited on silicon. Scale bar, 1 µm.

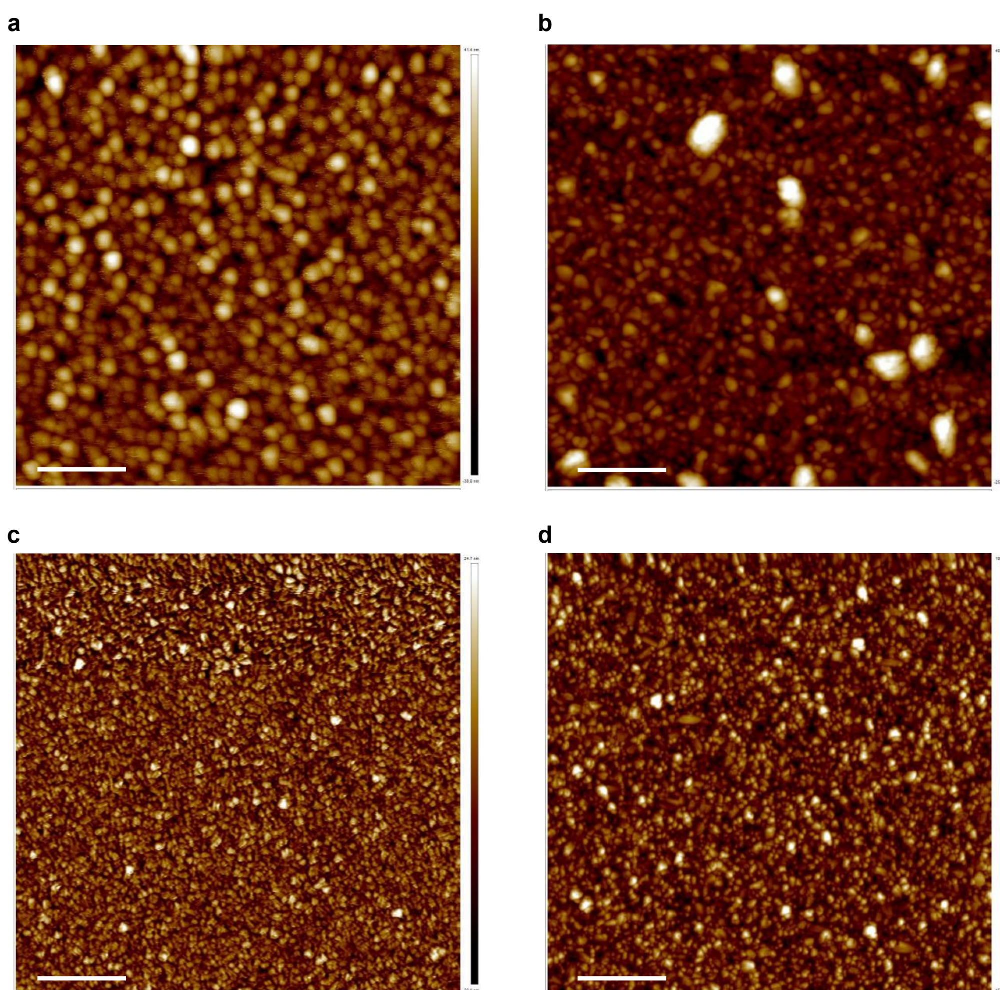

Supplementary Fig. 8 | Surface roughness of the alkylammonium cation-modified perovskite films. a-d, Atomic force microscopy (AFM) images of the control (**a**), MA (**b**), PEA (**c**) and *t*-BA (**d**) films deposited on silicon. Scale bar, 1 μm. The corresponding root-mean-square (RMS) surface roughness values are 11.2 nm, 6.95 nm, 5.06 nm and 4.13 nm, respectively.

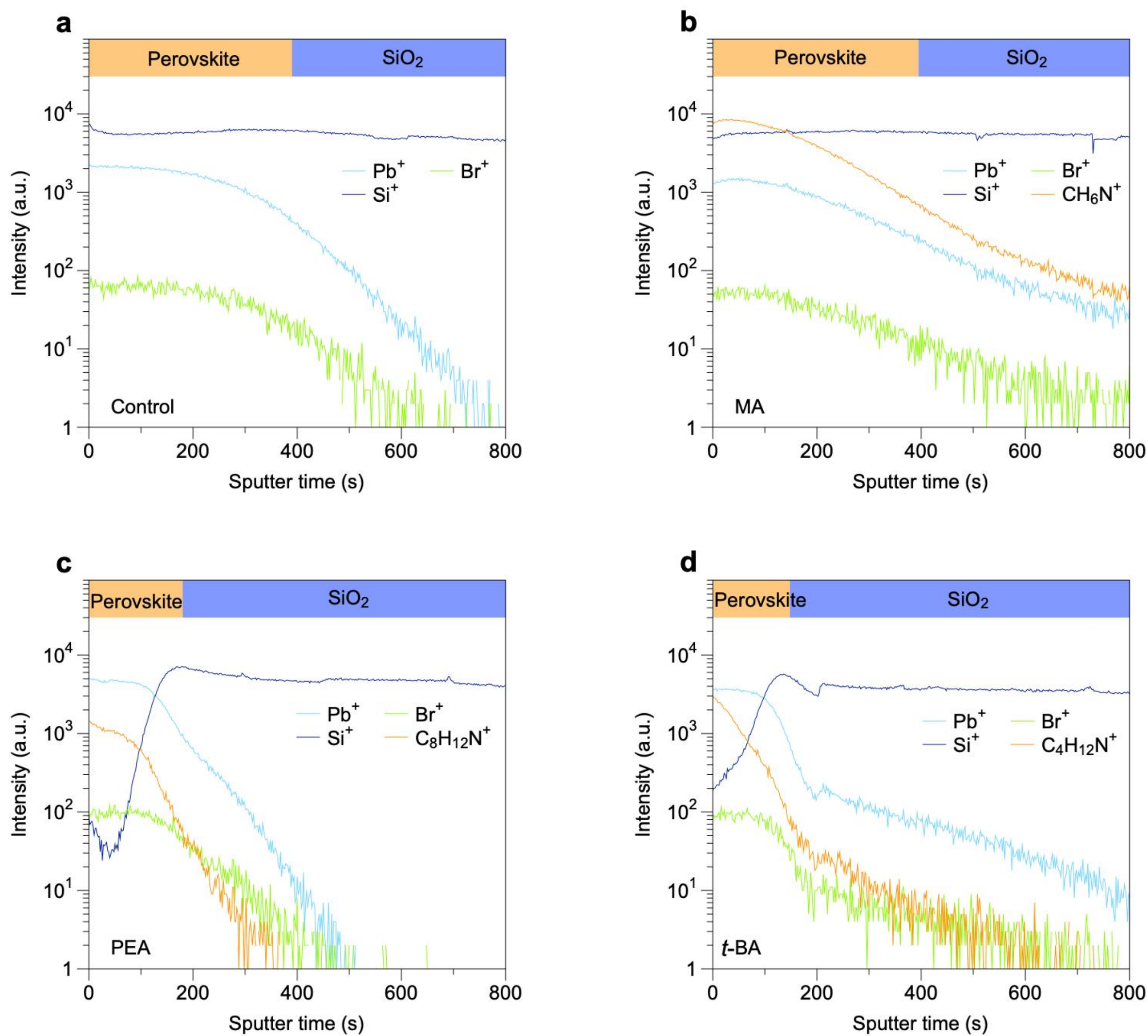

Supplementary Fig. 9 | Elemental depth analysis of the perovskite films. a-d, Time-of-flight secondary ion mass spectrometry (ToF-SIMS) depth profiles of the control (**e**), MA (**f**), PEA (**g**) and *t*-BA (**h**) films deposited on silicon.

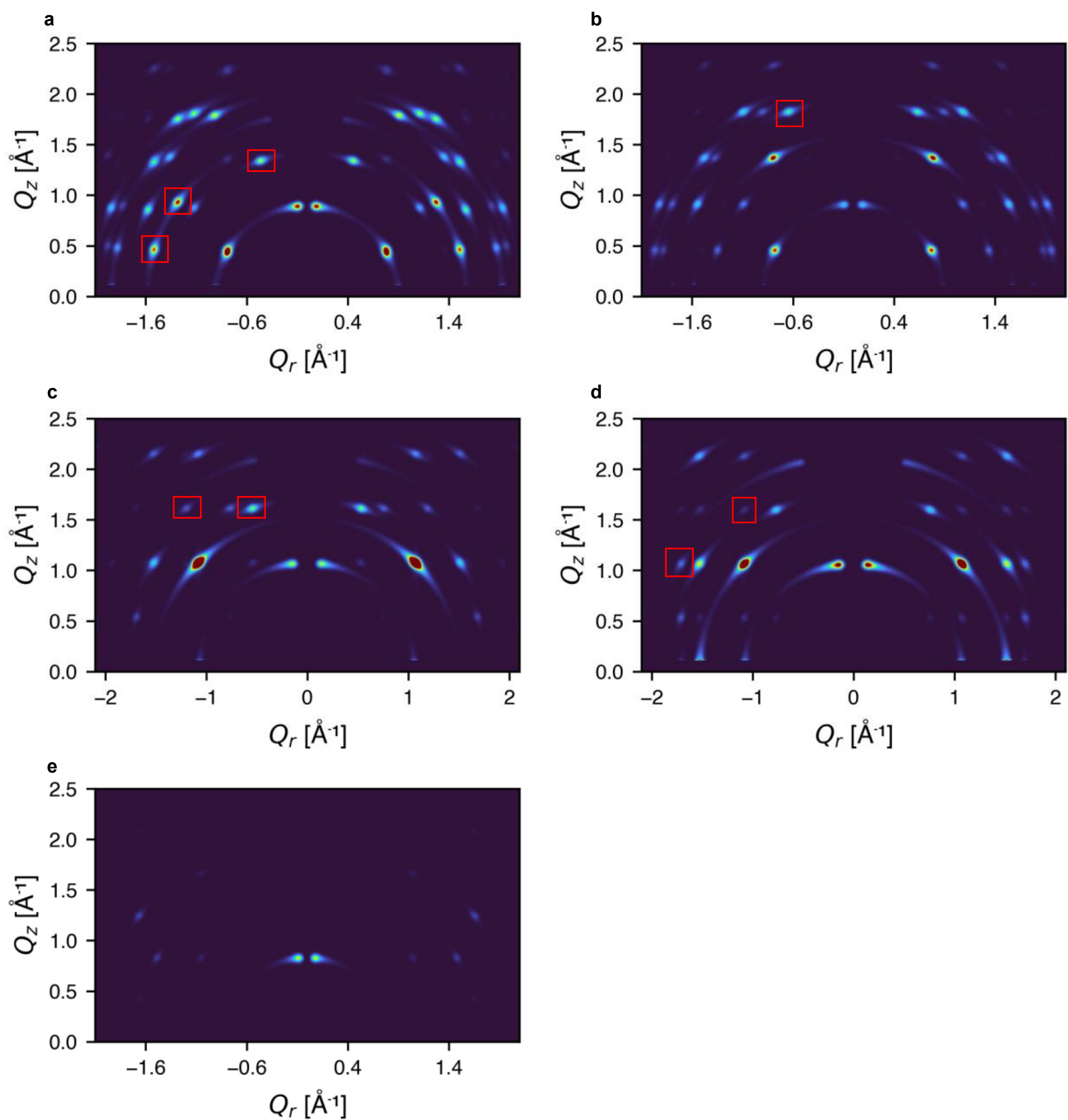

Supplementary Fig. 10 | Two-dimensional (2D) grazing-incidence wide-angle X-ray scattering (GIWAXS) simulations. a-e, Simulated 2D GIWAXS patterns for Cs_4PbBr_6 (102) (**a**) and (210) (**b**) orientations, and $CsPbBr_3$ (110) (**c**) and (002) (**d**) orientations and $CsPb_2Br_5$ (002) orientation (**e**). All results were simulated as uniaxial orientations, and texture directions were selected based on strong out-of-plane oriented peaks in each case (generally the lowest angle peak), and where the relevant, characteristic Bragg spots for that orientation are marked.

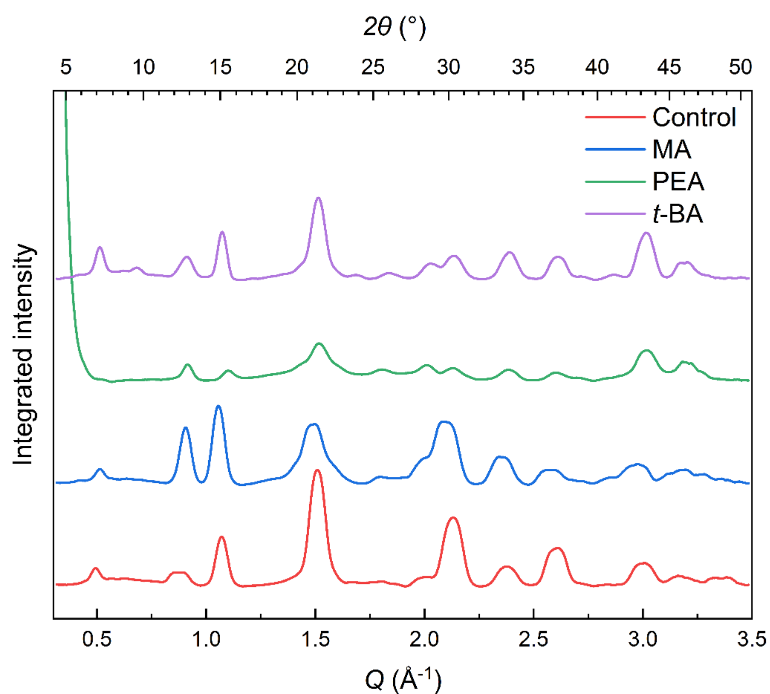

Supplementary Fig. 11 | Integrated GIWAXS. Azimuthally integrated one-dimensional (1D) GIWAXS scattering from the control (**a**), MA (**b**), PEA (**c**), *t*-BA (**d**) films on silicon. A large specular reflection peak is observed at low angles from the PEA film (see Extended Data Fig. 2e) owing to its low roughness.

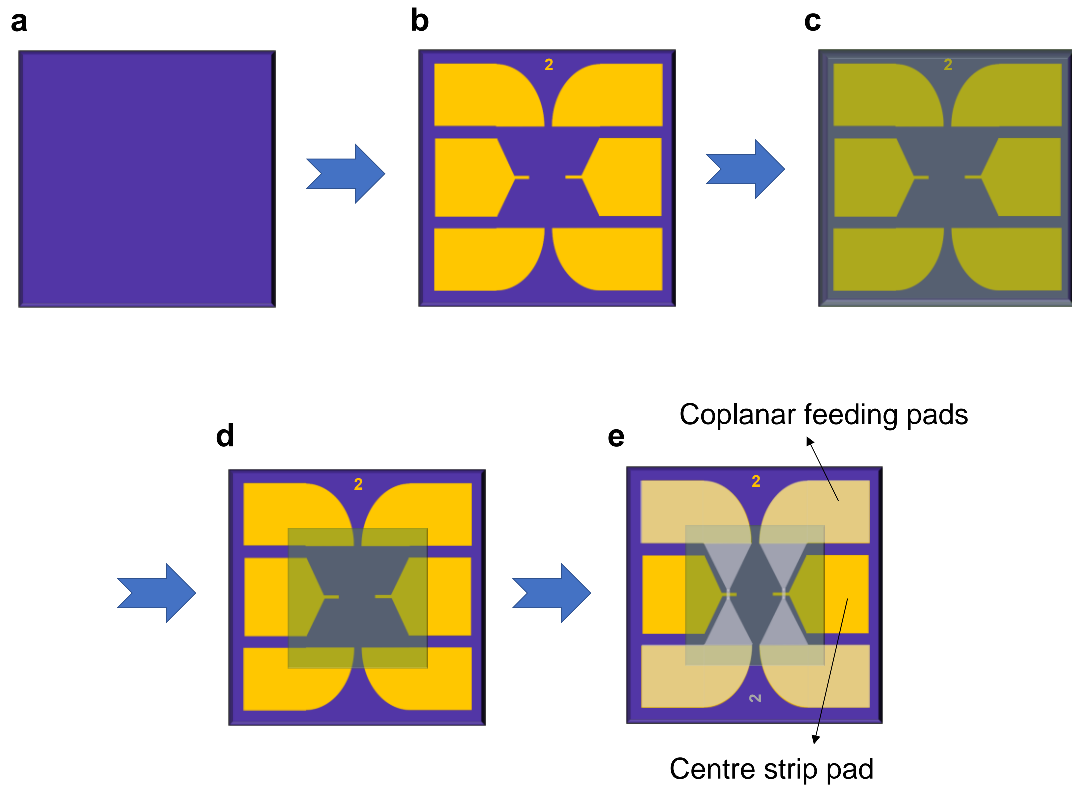

Supplementary Fig. 12 | Device design and fabrication. a, Substrate cleaning. **b**, Deposition of the bottom electrodes (all-refection Au films). **c**, Deposition of the perovskite and functional layers. **d**, Exposure of the bottom electrodes. **e**, Deposition the top electrodes (semi-transparent Ag films). The device active area is defined by the overlap of the centre Au strip and Ag coplanar waveguide feeding pads. This coplanar configuration of the perovskite sources on silicon not only permits the reflection effect but also enables monolithic integration with other photonic components[6].

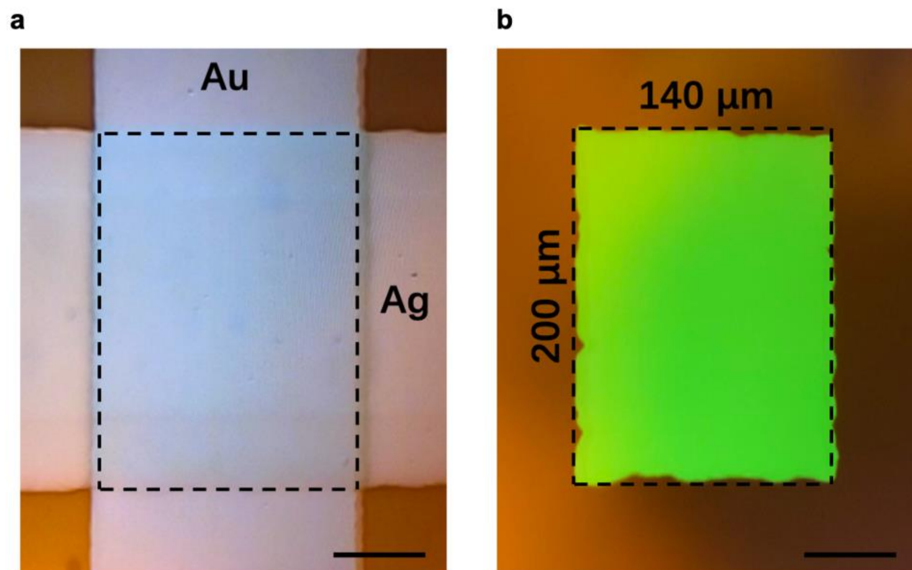

Supplementary Fig. 13 | Microscope images of a single pixel. a,**b**, The overlap area of the pixel measured under a bright-field mode (**a**), and a dark-field mode with a forward bias (**b**). Scale bar, 50 µm.

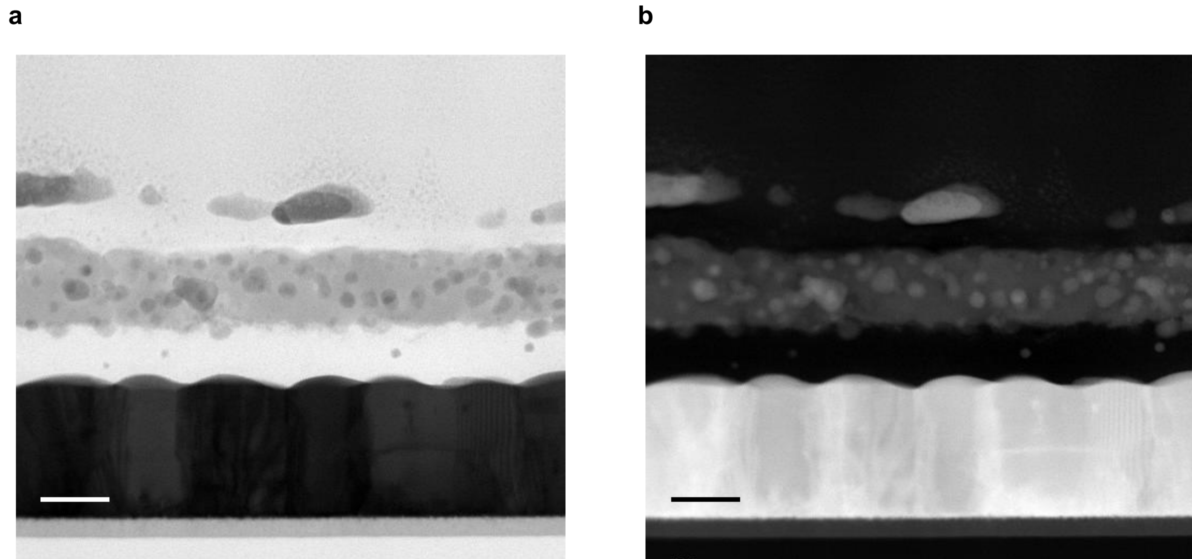

Supplementary Fig. 14 | Scanning transmission electron microscopy (STEM) of a *t*-BA device. a-b, Bright-field image (**a**) and annular dark-field image (**b**) of the *t*-BA device. The grain boundaries of the perovskite emissive layer are not resolved exhibiting a uniform, compact and pinhole-free film coverage. Scale bar, 50 nm.

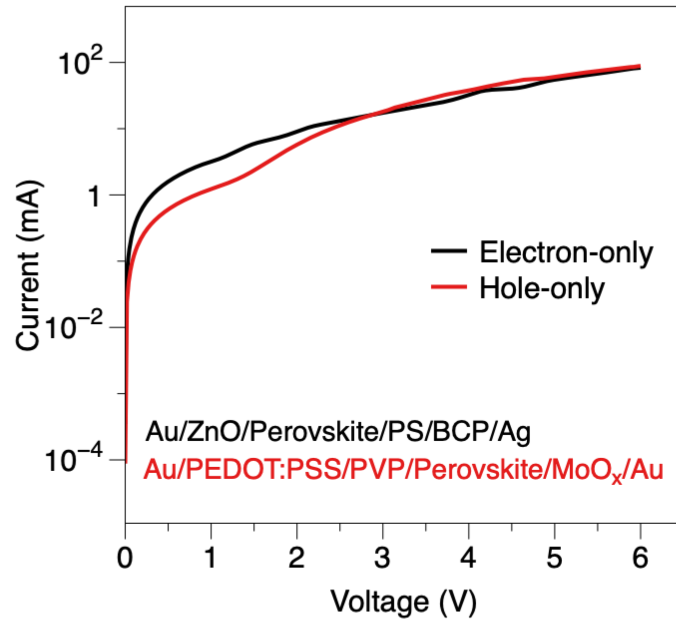

Supplementary Fig. 15 | Optimisation of electron and hole injections. Current density–voltage (*J*–*V*) curves of the optimised electron-only (Au/ZnO/perovskite/polystyrene (PS)/bathocuproine (BCP)/Ag) and hole-only (Au/PEDOT:PSS/polyvinylpyrrolidone (PVP) /perovskite/MoO_x/Au) devices. The thickness of PEDOT:PSS (40 nm), BCP (20 nm), PVP (5 nm) and PS (5 nm) layers were carefully tunned for obtaining a balanced charge injection.

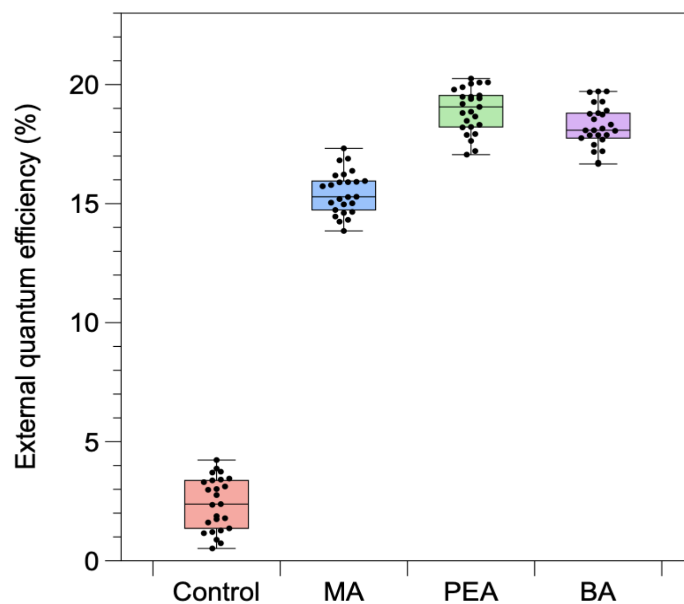

Supplementary Fig. 16 | EQEs of the perovskite sources. Box and whisker plots of EQEs for the control, MA, PEA and *t*-BA devices. The data points of each boxplot were collected from 25 devices. Data are shown as box and whisker plots. The bounds of the box plot indicate the 25th and 75th percentiles, the centre line indicate average, the bar indicates medians, and the whiskers indicate minima and maxima.

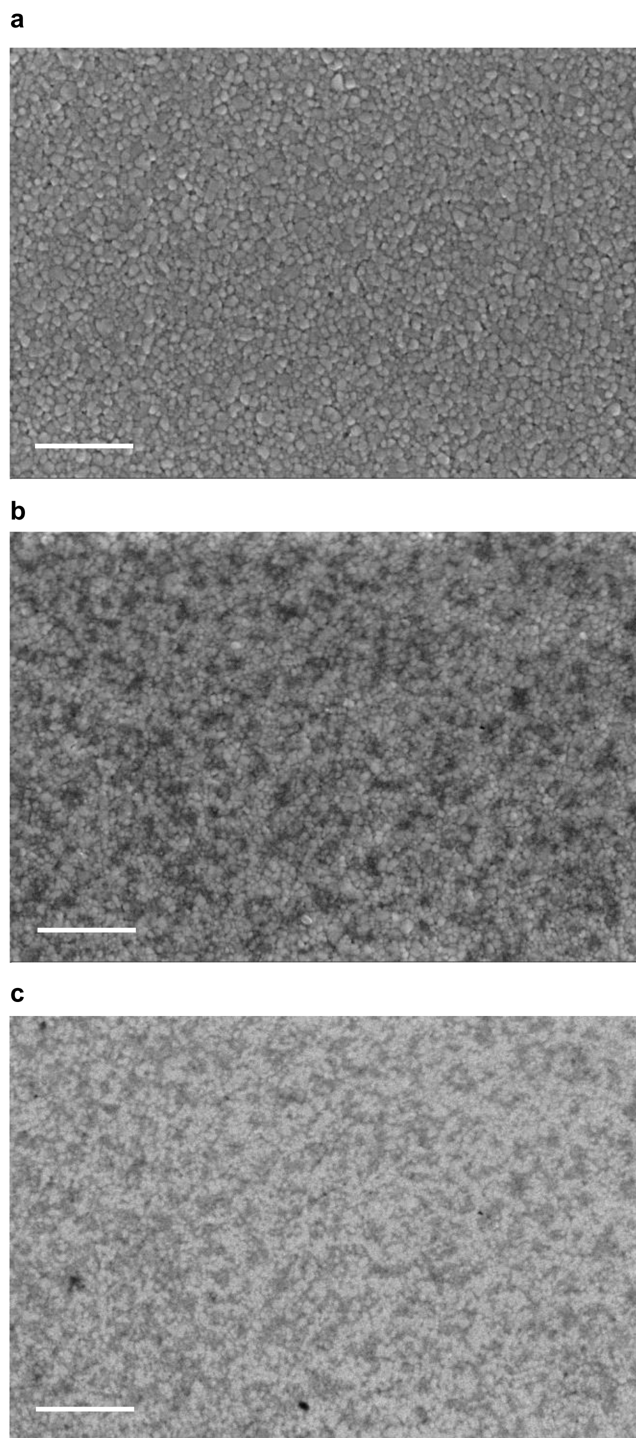

Supplementary Fig. 17 | Surface passivation of the perovskite films. a, **b**, SEM images of the *t*-BA films without (**a**) and with a PS capping layer (**b**). **c**, Backscattered electrons image of the *t*-BA film with a PS capping layer. The chemically inert and highly hydrophobic PS capping layer effectively passivates the localised grain boundaries. Scale bar, 1 µm.

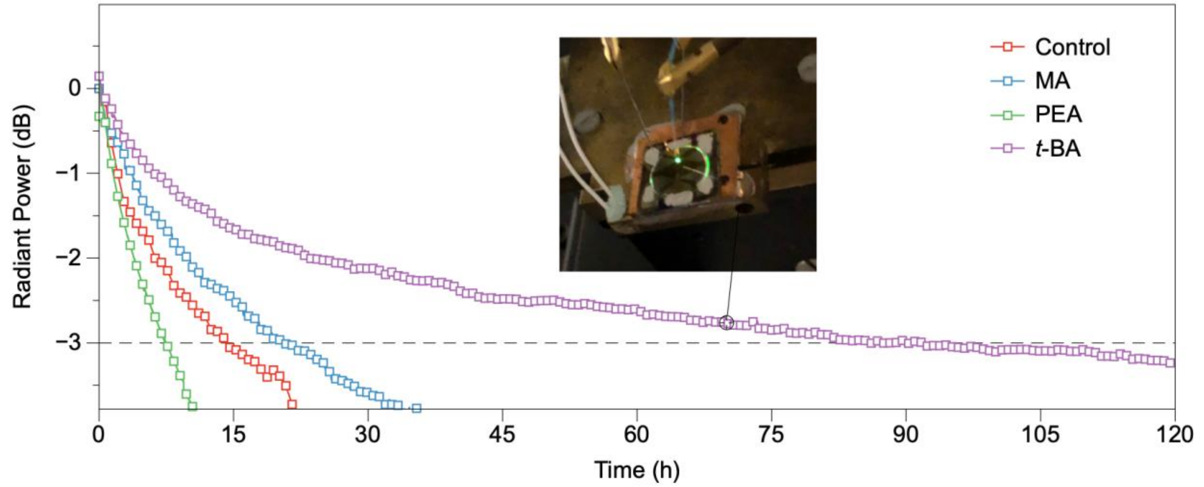

Supplementary Fig. 18 | Long-term radiant power tracking test. Radiant power (dB) as a function of time was tracked for the control, MA, PEA and *t*-BA devices with a constant driving current of 50 μA (~177 mA cm^{-2}). The -3 dB lifetime (defined as the time taken for the received power to decrease to half of the initial radiant power) was estimated to be 15.3, 23.2, 7.5 and 87.8 hours for the control, MA, PEA and *t*-BA devices, respectively, measured at room temperature without an external thermal dissipation setup, respectively. Inset: photograph of the best-performance *t*-BA device operating after ~70 hours.

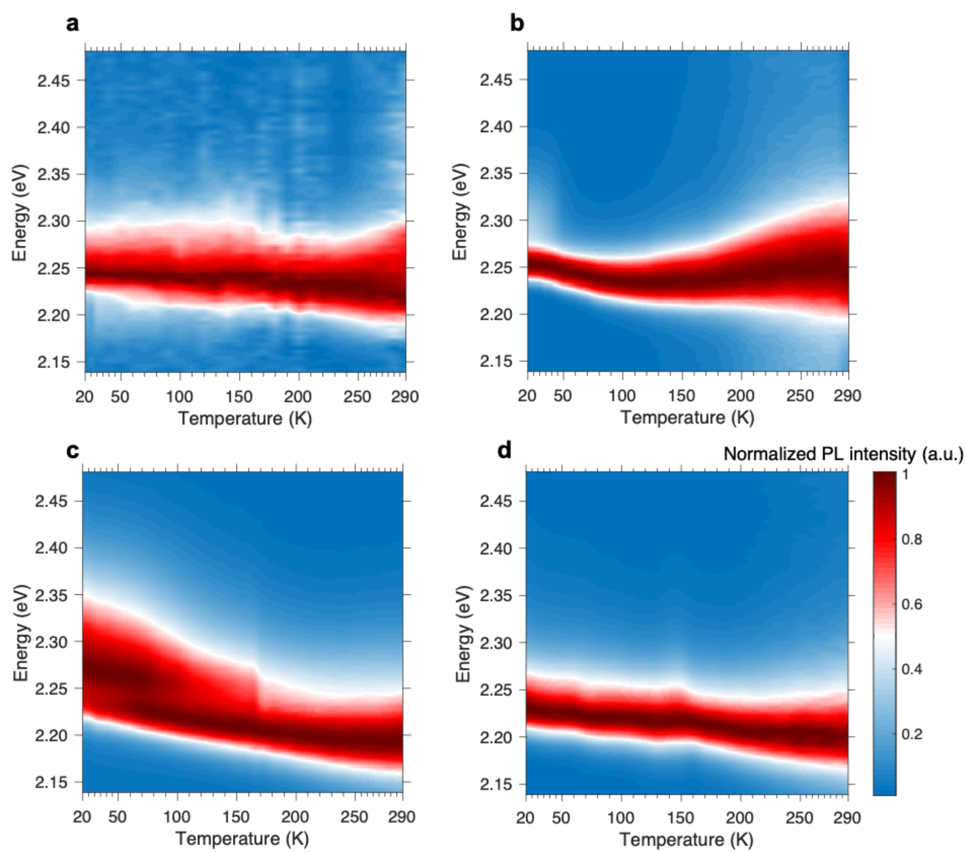

Supplementary Fig. 19 | Temperature dependence of steady-state PL spectra. Normalised steady-state PL spectra of the control (**a**), MA (**b**), PEA (**c**), and *t*-BA (**d**) films at temperatures between 20 and 290 K.

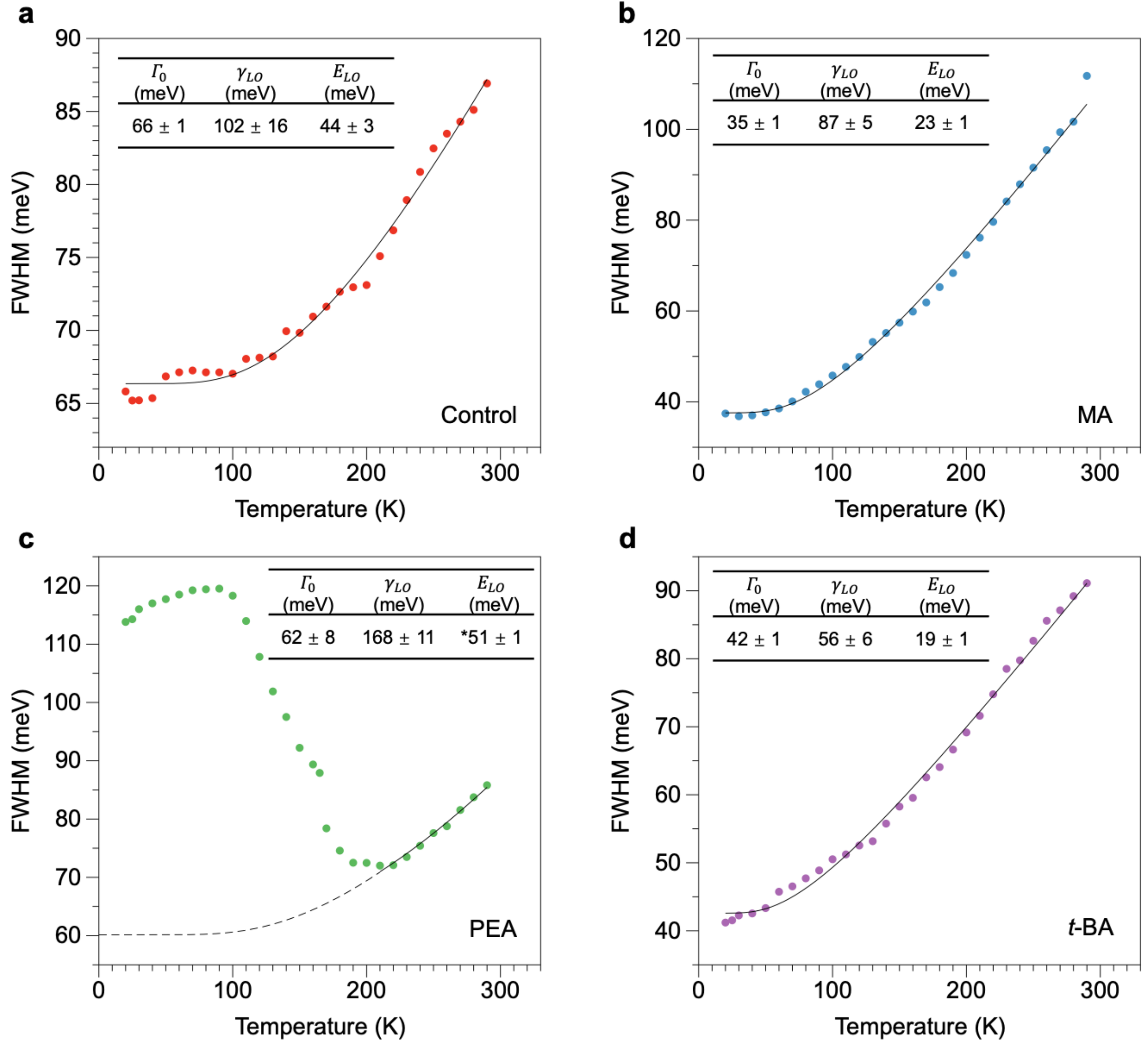

Supplementary Fig. 20 | Temperature dependence of PL linewidth. FWHM of the steady-state PL spectra as a function of temperature for the control (**a**), MA (**b**), PEA (**c**), and *t*-BA (**d**) films. The solid lines are fitted based on Supplementary Note 3, which account for contributions from the Fröhlich coupling with LO phonons and inhomogeneous broadening. The inserts are the derived linewidth parameters of the perovskite films. For fits to the data from the PEA films, the value of E_{LO} is derived by the same method as the other group of the perovskite films used (fits were only carried out between 200 and 290 K)[7].

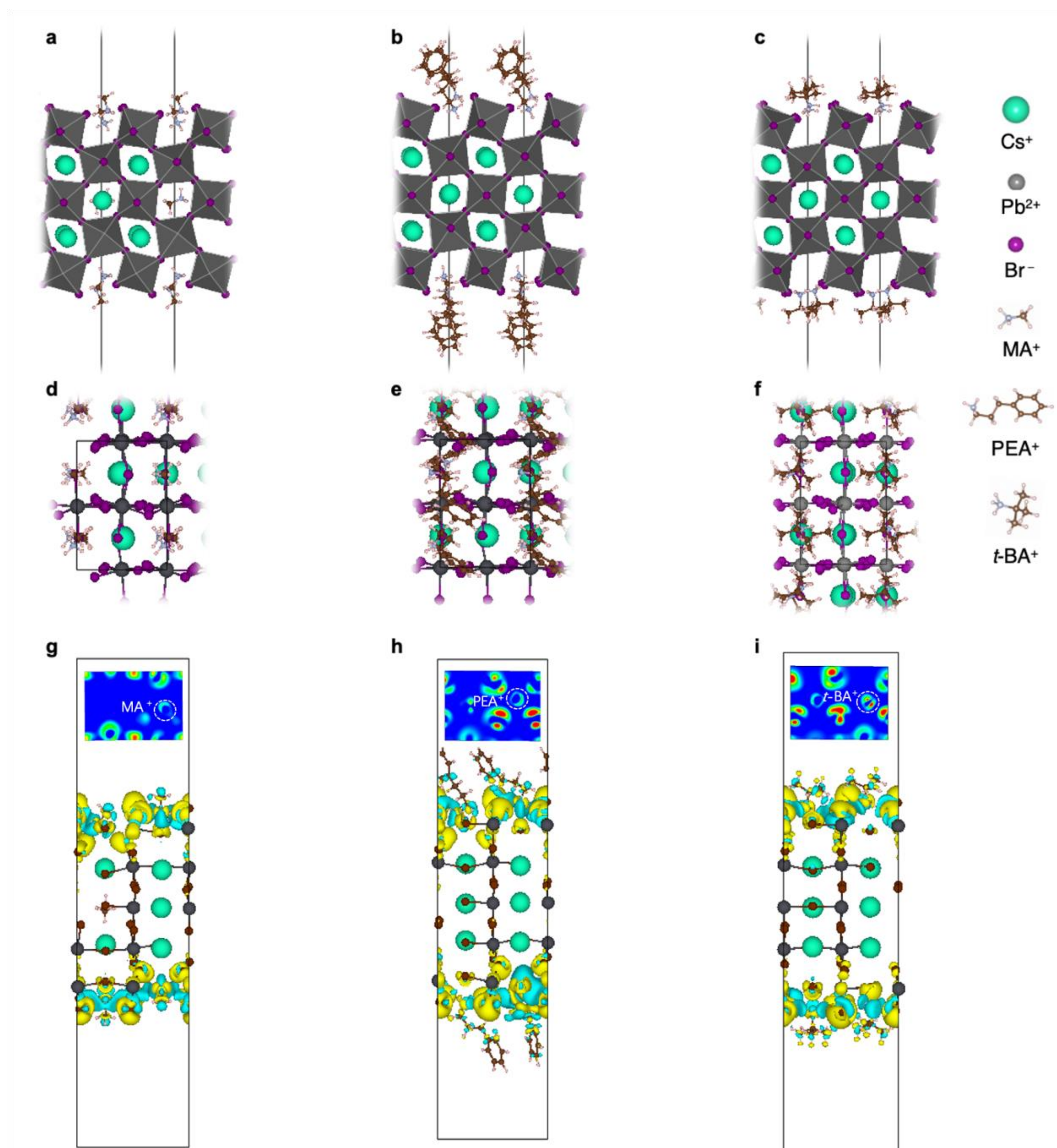

Supplementary Fig. 21 | Density functional theory (DFT) calculations of the organic cation-modified $CsPbBr_3$ perovskite surfaces. The optimised supercell structures, top views and differential charge density for the adsorption of the MA (**a**, **d**, and **g**), PEA (**b**, **e**, and **h**) and *t*-BA (**c**, **f**, and **i**) cations on the $CsPbBr_3$ surface, respectively. The inserts in **g**-**i**: 2D differential charge density profiles.

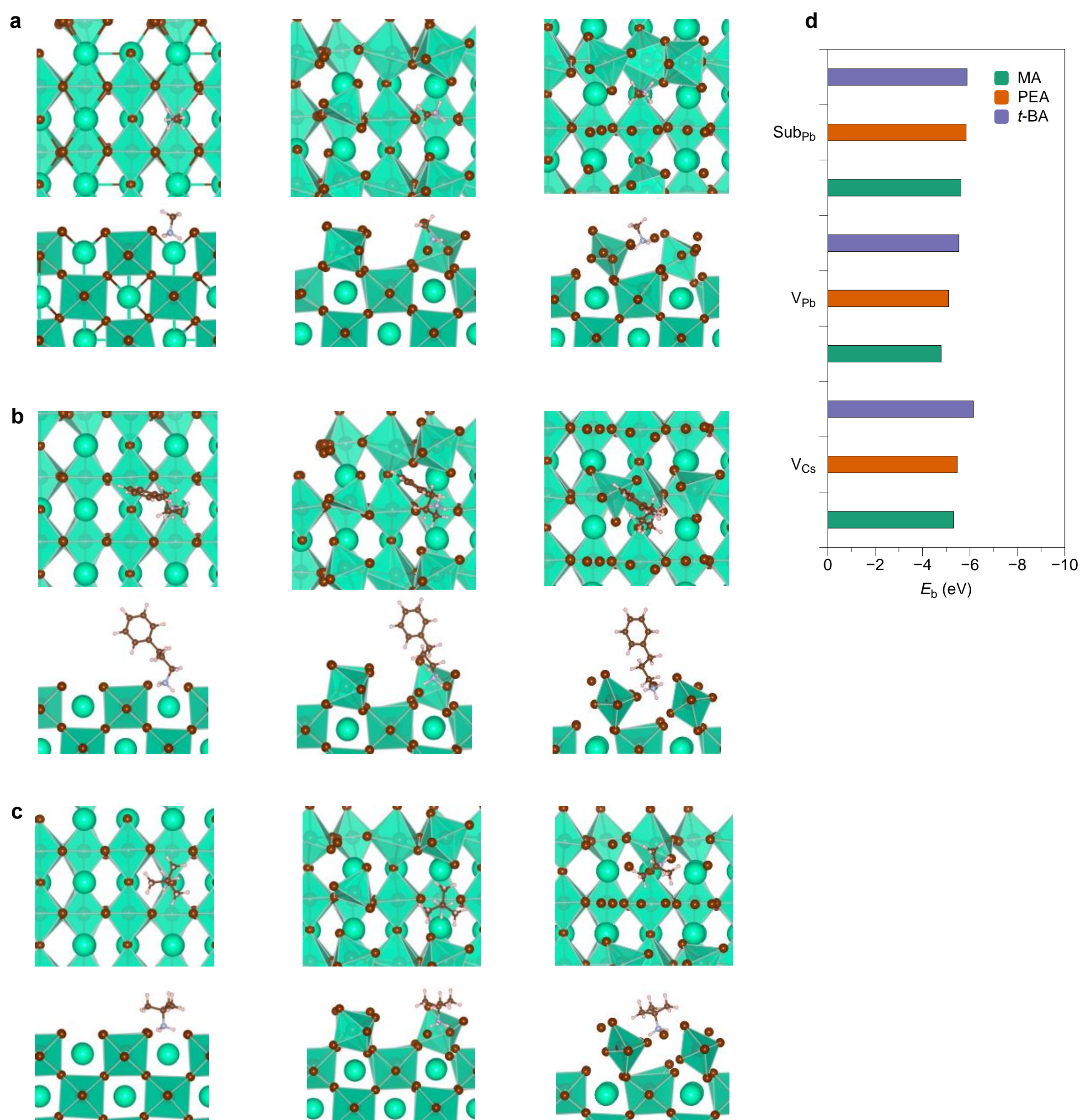

Supplementary Fig. 22 | Interactions between the organic cations and perovskite defects. Top view (top panels) and side view (down panels) illustrations of the interactions between the MA (**a**), PEA (**b**) and *t*-BA (**c**) cations with the point defects, including Cs-site and Pb-site vacancies and Pb-site substitutions. (**d**) Binding energy (E_b) profiles of the organic cations with defects.

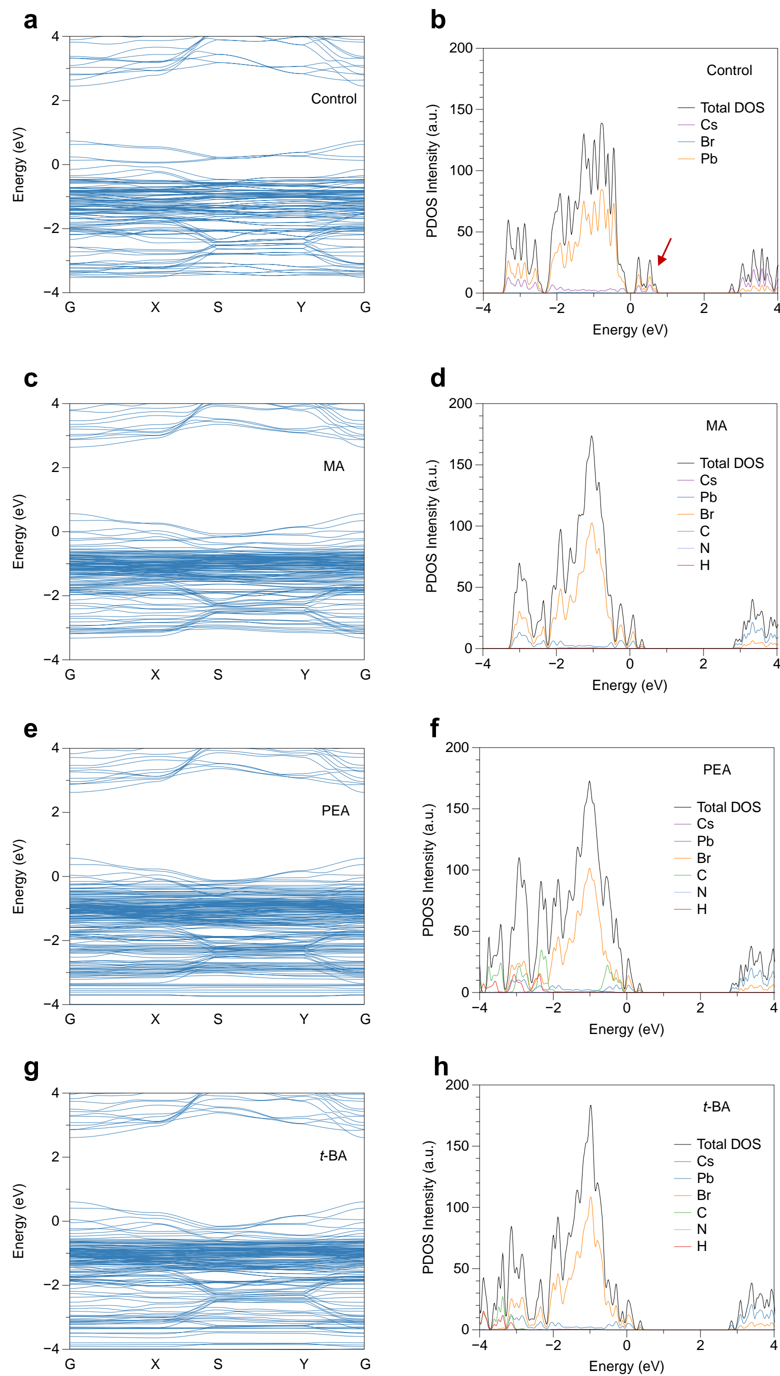

Supplementary Fig. 23 | Electronic density of states of the organic cation-modified $CsPbBr_3$. Calculated band structures and projected density of states (PDS) of the control (**a**, **b**), MA (**c**, **d**), PEA (**e**, **f**) and *t*-BA (**g**, **h**) perovskites. The zero energy is set to the Fermi level. The in-gap states of $CsPbBr_3$ highlighted with a red arrow.

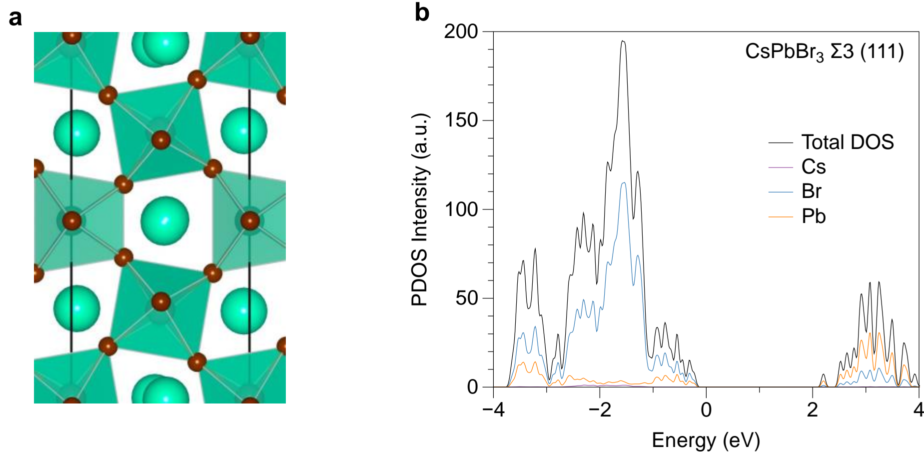

Supplementary Fig. 24 | Electronic density of states of grain boundary structure in $CsPbBr_3$. Optimised geometries (**a**) and PDOS (**b**) of Σ3 (111) grain boundaries. The zero energy is set to the Fermi level.

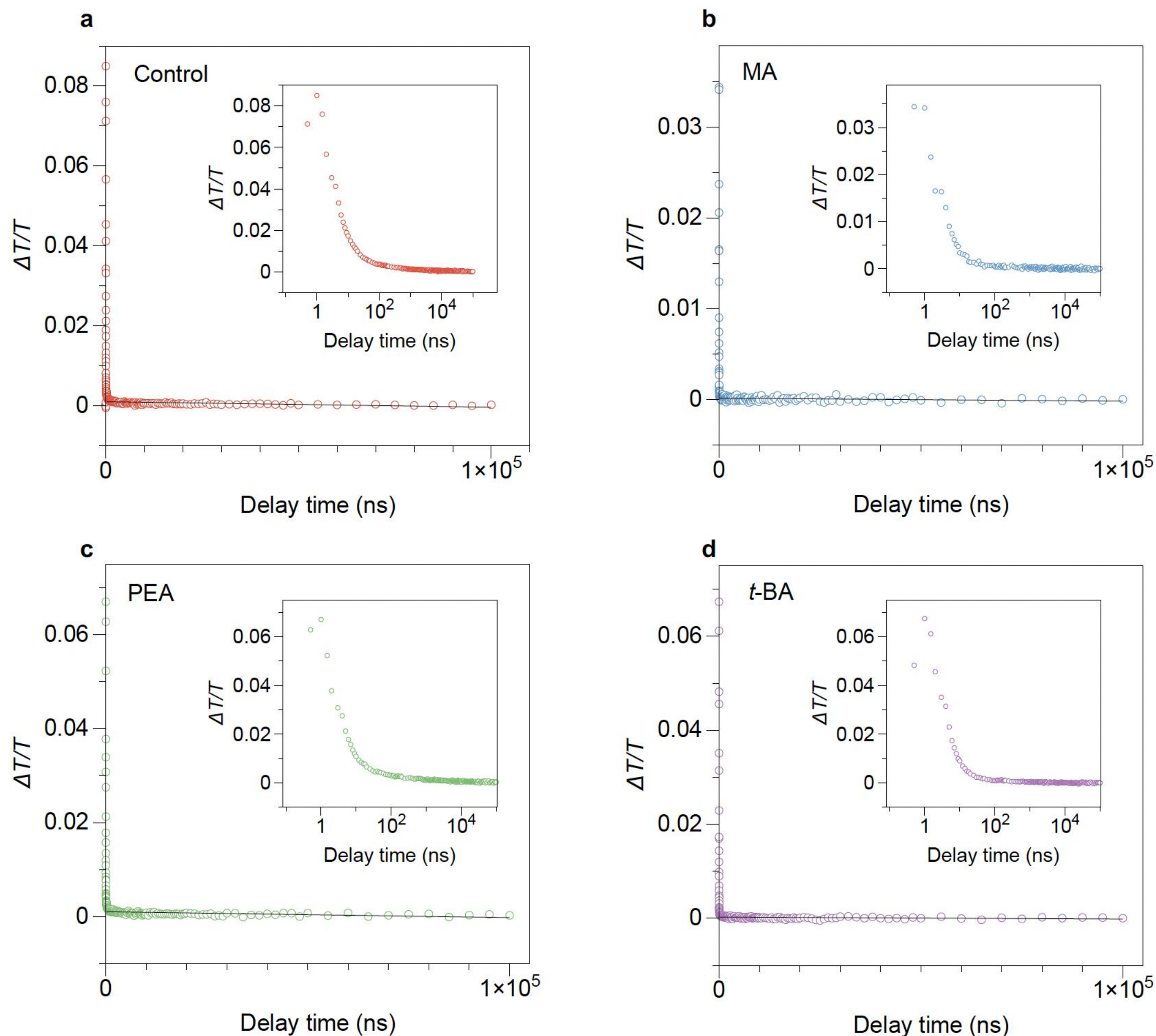

Supplementary Fig. 25 | Nanosecond-to-microsecond TA kinetics. a-d, Kinetics of the ground state bleach (GSB) of the control (**a**), MA (**b**), PEA (**c**) and *t*-BA (**d**) films. Solid lines are the rate equation fits in the tail regions (from 200 ns to 100000 ns) for the derivation of the k_1 values. Inserts are the bleaching kinetics with a logarithmic scale.

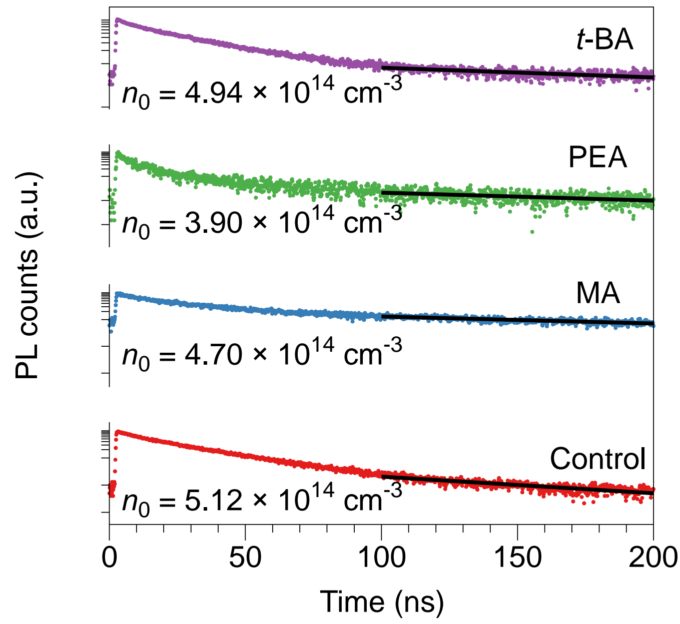

Supplementary Fig. 26 | Low-fluence transient PL kinetics. TRPL decay transients of the control, MA, PEA, *t*-BA films at low excitation fluences. The k_1 values were extracted from exponential fits in the tail regions of the TRPL decay transients (100-200 ns) at low-fluence excitations (solid lines).

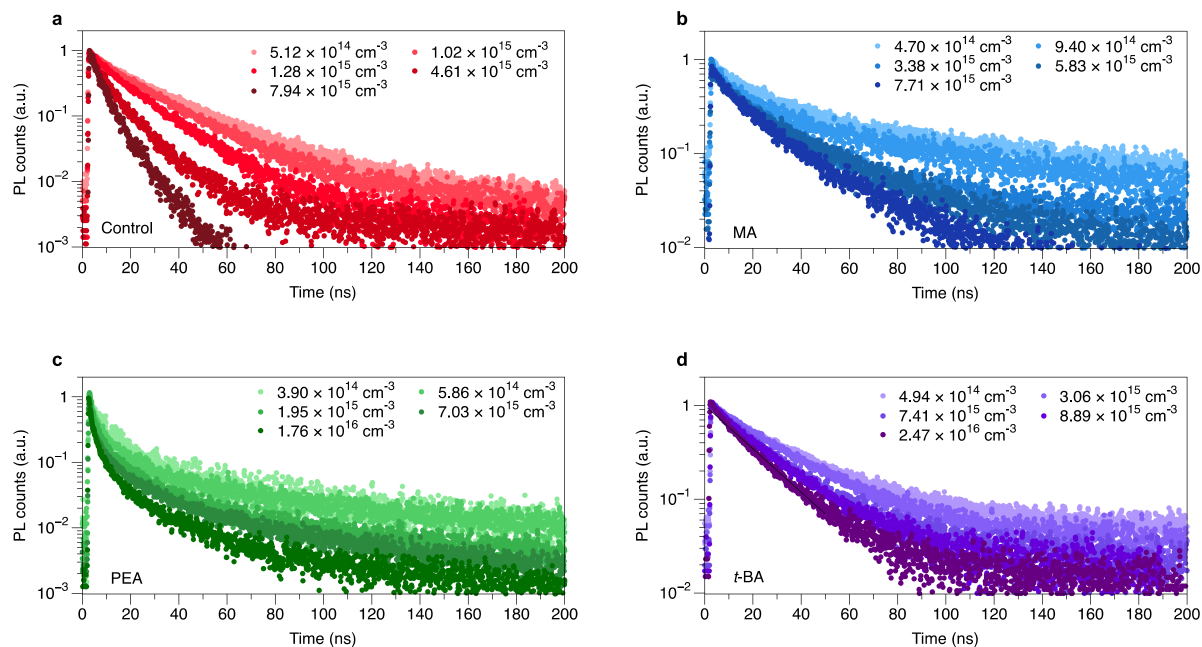

Supplementary Fig. 27 | Fluence-dependent transient PL kinetics. a-d, TRPL decays of the control (**a**), MA (**b**), PEA (**c**) and *t*-BA (**d**) films.

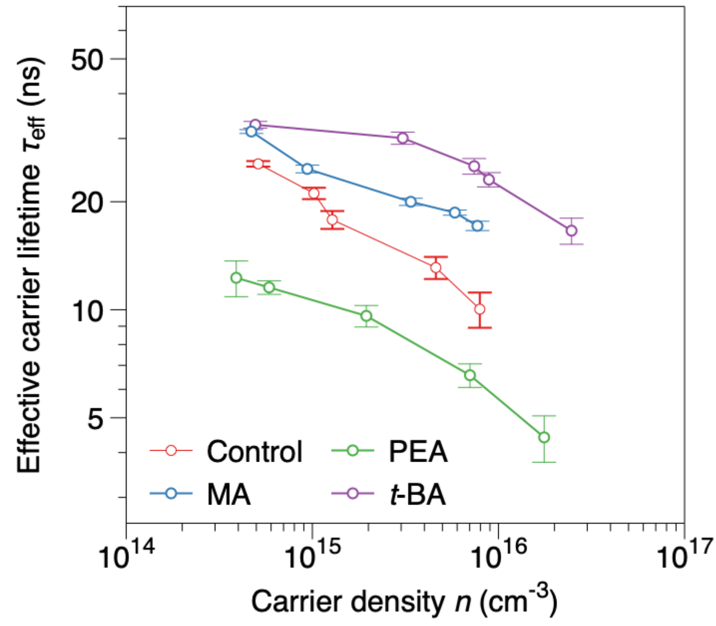

Supplementary Fig. 28 | The τ_{eff} as a function of photon-injected carrier density. Data are presented as best-fit parameters with error bars indicating the 95% confidence intervals of the τ_{eff} value fits (single-exponential fit).

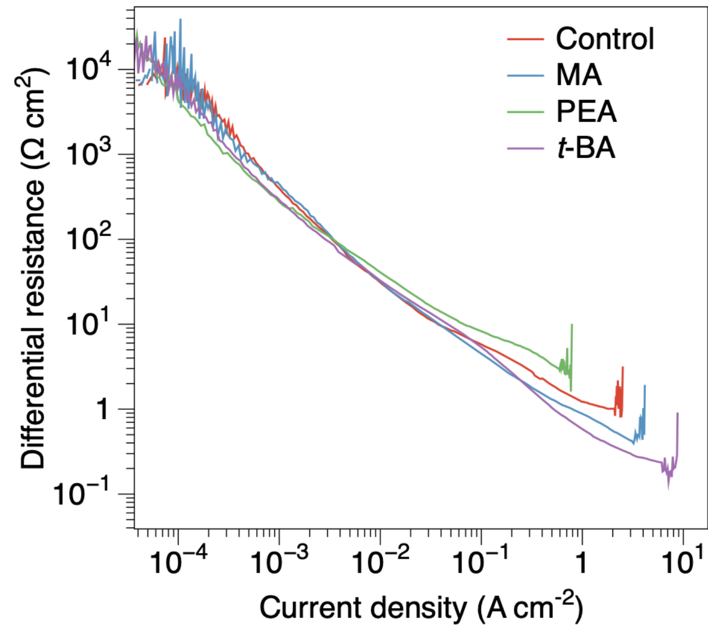

Supplementary Fig. 29 | Device differential resistance characteristics. Differential resistance of the control, MA, PEA and *t*-BA devices as a function of current density.

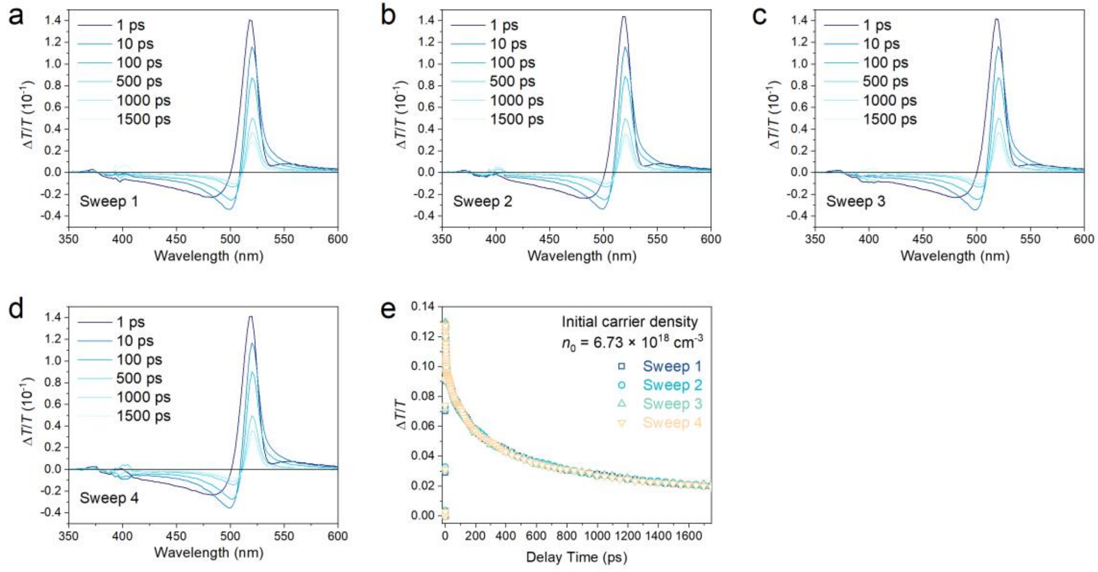

Supplementary Fig. 30 | TA kinetics of individual sweeps of the *t*-BA samples. a-d, Spectra and kinetics (516 to 526 nm) of individual sweeps from the beginning to the end of the overall measurement. **e**, Bleaching dynamics of the *t*-BA films monitored near the absorption onsets. No systematic difference is observed in the spectra and kinetics from the first sweep to the last sweep, indicating that there is no noticeable laser-induced degradation during the measurements.

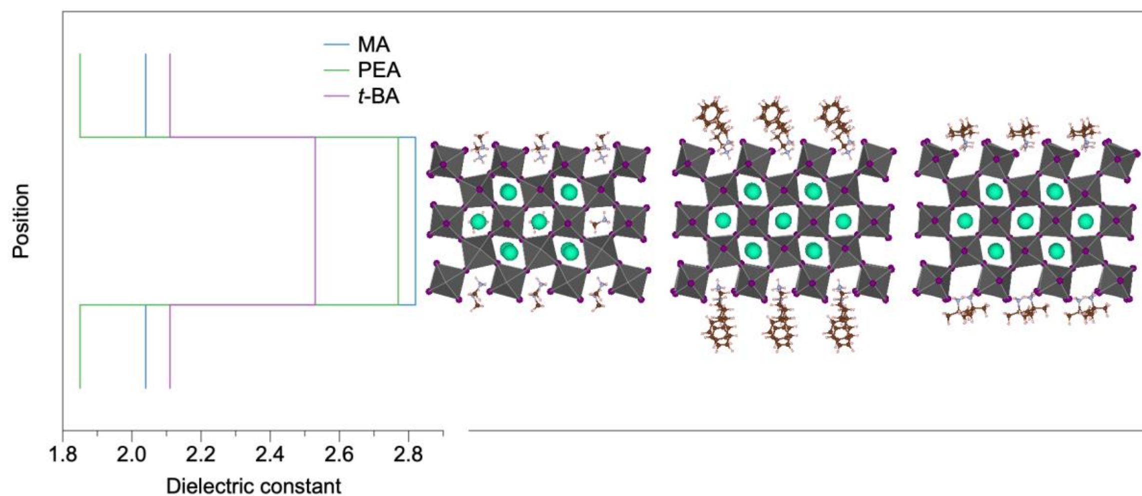

Supplementary Fig. 31 | Calculated dielectric profiles of the organic cation-modified $CsPbBr_3$. The *x*-axis represents the dielectric constants of the cation layers and inorganic layers. On the right is the crystal structure of the MA, PEA and *t*-BA modified $CsPbBr_3$, respectively.

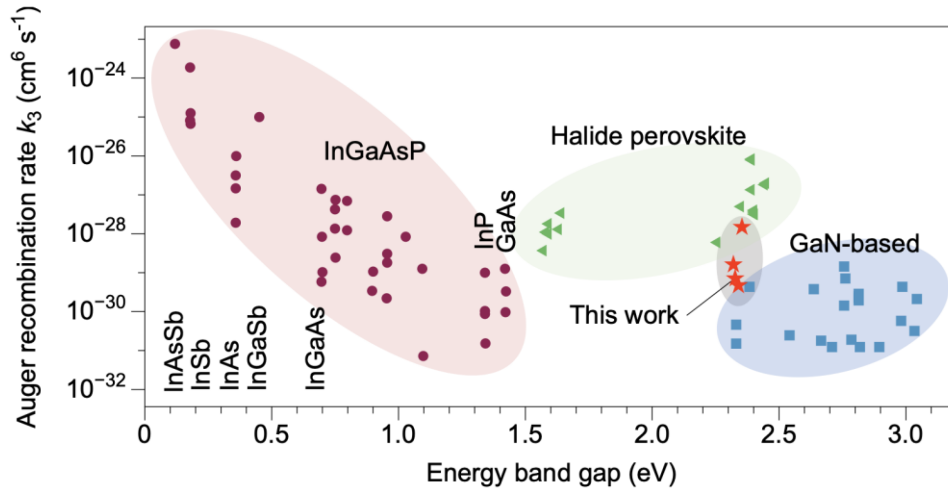

Supplementary Fig. 32 | Summary of the reported Auger recombination rate constants for various materials[2,8–13]. Long wavelength emitters (circles); short-wavelength GaN-based emitters (rectangles); halide perovskite emitters (triangles). Apart from PL properties, the main significant parameter that we find varies most in the *t*-BA films is the enhanced charge-carrier mobility due to the reduced phonon scattering. In nitride quantum well LED structures, previous studies have demonstrated the occurrence of defect-assisted Auger recombination[14,15], where enhanced charge carrier scattering leads to enhanced indirect Auger recombination. We hypothesise that a similar process takes place in our metal halide perovskite composites, where the low charge carrier scattering within the 3D perovskite domains of the *t*-BA films may also be responsible for the low k_3 value and the corresponding ability of the devices to drive effectively under high current densities.

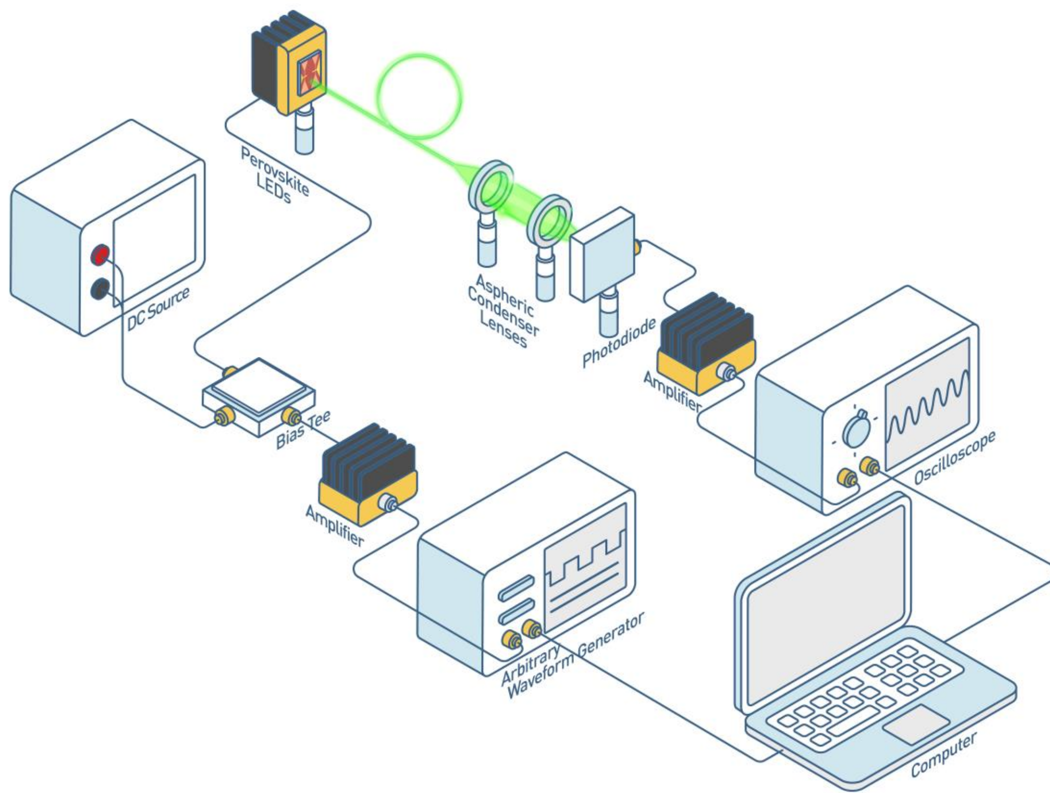

Supplementary Fig. 33 | Setup of the modulation performance measurement. Schematic illustration of the data transmission measurement system used in this work.

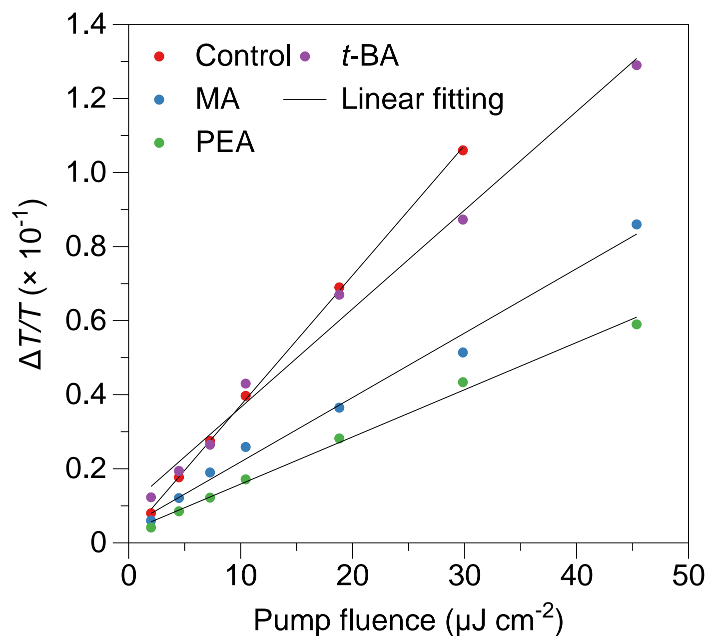

Supplementary Fig. 34 | Pump-intensity dependent TA kinetics. Femtosecond-to-nanosecond TA signals versus excitation fluences. From the relation between TA signals ($\Delta T/T$) and pump fluences used in the TA measurements for different perovskite films, we confirm that no significant nonlinear processes (such as two-photon absorption) were involved. Carrier densities increase linearly with pump fluences, which is essential for accurate determination of rate constants.

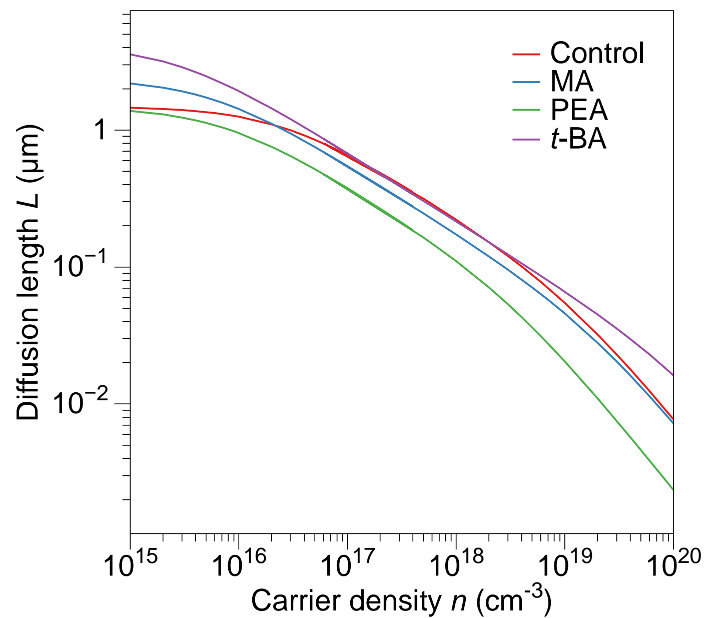

Supplementary Fig. 35 | Carrier diffusion length calculations. Carrier diffusion length L as a function of carrier density n for the perovskite films.

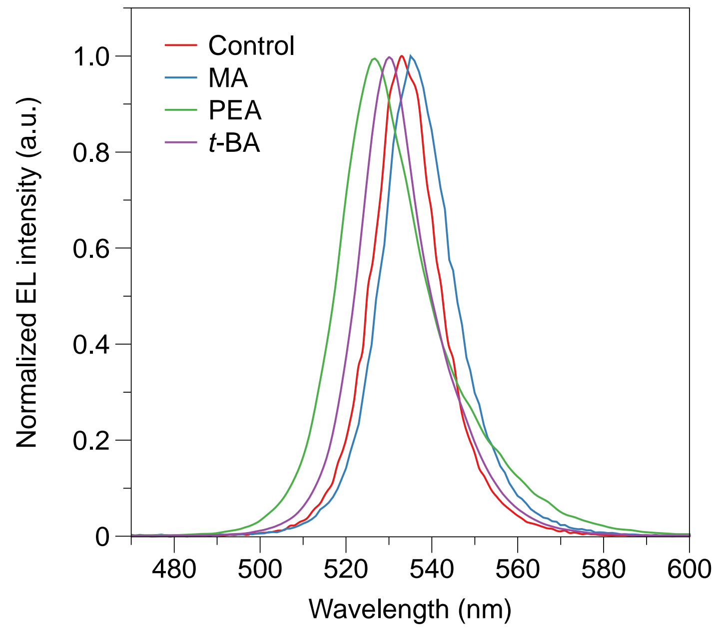

Supplementary Fig. 36 | EL emission characteristics. The normalised EL spectra of the LED sources.

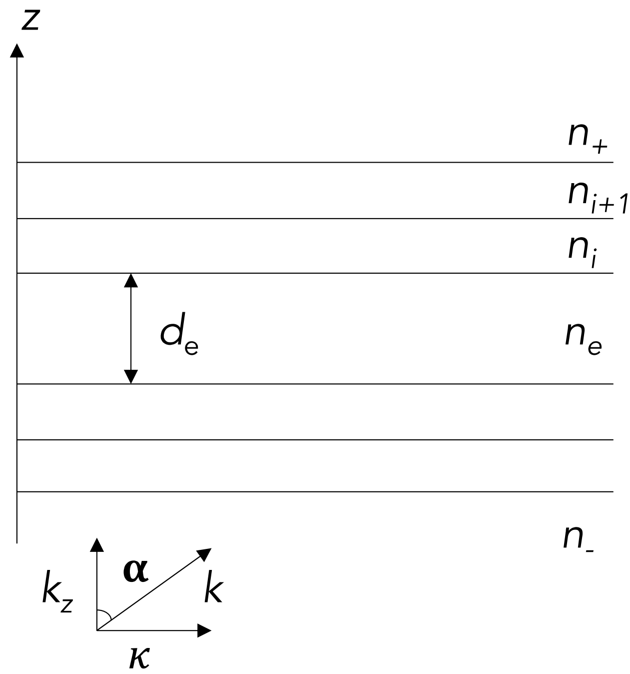

Supplementary Fig. 37 | Structure of the multilayer film in the optical simulation. The *e*-th layer represents the emitting medium, ± is labelled as the outmost layer in either +z or -z direction.

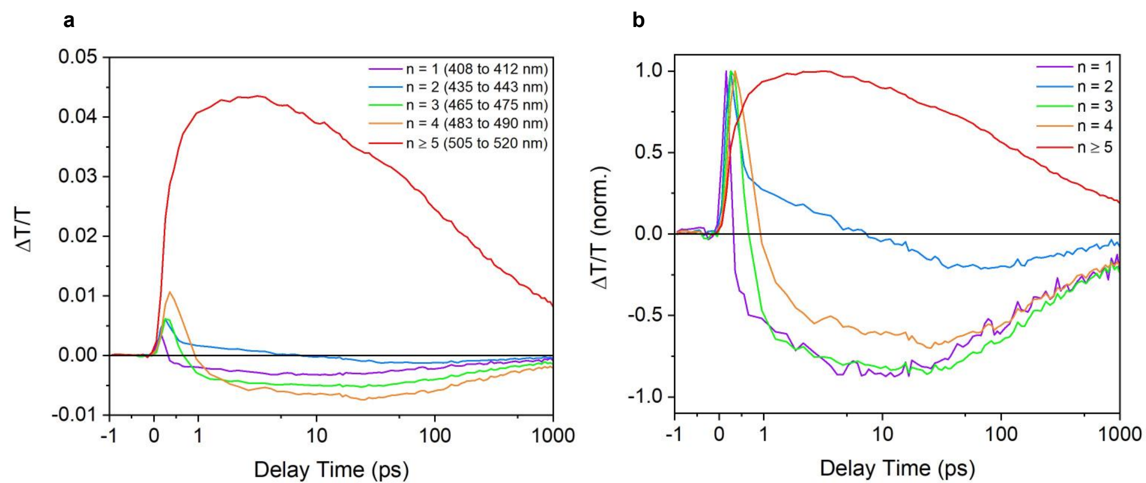

Supplementary Fig. 38 | TA spectra of the PEA film. a-b, Initial (**a**) and normalised (**b**) TA spectra probed at selected wavelengths corresponding to the distinct bleaching lines (n=1, 2, 3, 4, ≥5) as a function of delay time.

References

1. Green, R. P. *et al.* Modulation bandwidth studies of recombination processes in blue and green InGaN quantum well micro-light-emitting diodes. *Applied Physics Letters* **102**, 1–5 (2013).
2. Richter, J. M. *et al.* Enhancing photoluminescence yields in lead halide perovskites by photon recycling and light out-coupling. *Nature Communications* **7**, 13941 (2016).
3. Davies, C. L. *et al.* Temperature-Dependent Refractive Index of Quartz at Terahertz Frequencies. *Journal of Infrared, Millimeter, and Terahertz Waves* **39**, 1236–1248 (2018).
4. Wehrenfennig, C., Eperon, G. E., Johnston, M. B., Snaith, H. J. & Herz, L. M. High Charge Carrier Mobilities and Lifetimes in Organolead Trihalide Perovskites. *Advanced Materials* **26**, 1584–1589 (2014).
5. Anaya, M. *et al.* Best practices for measuring emerging light-emitting diode technologies. *Nature Photonics* **13**, 818–821 (2019).
6. Wen, C. P. Coplanar Waveguide, a Surface Strip Transmission Line Suitable for Nonreciprocal Gyromagnetic Device Applications. *1969 G-MTT International Microwave Symposium* 110–115 (1969) doi:10.1109/GMTT.1969.1122668.
7. Wright, A. D. *et al.* Electron–phonon coupling in hybrid lead halide perovskites. *Nature Communications* **7**, 11755 (2016).
8. PIPREK, J. Carrier Transport. in *Semiconductor Optoelectronic Devices* 49–82 (Elsevier, 2003). doi:10.1016/B978-0-08-046978-2.50028-4.
9. Piprek, J., Römer, F. & Witzigmann, B. On the uncertainty of the Auger recombination coefficient extracted from InGaN/GaN light-emitting diode efficiency droop measurements. *Applied Physics Letters* **106**, 101101 (2015).
10. Wehrenfennig, C., Eperon, G. E., Johnston, M. B., Snaith, H. J. & Herz, L. M. High Charge Carrier Mobilities and Lifetimes in Organolead Trihalide Perovskites. *Advanced Materials* **26**, 1584–1589 (2014).
11. Ban, M. *et al.* Solution-processed perovskite light emitting diodes with efficiency exceeding 15% through additive-controlled nanostructure tailoring. *Nature Communications* **9**, 1–10 (2018).
12. Jiang, Y. jpclett. 5b02290. pd. *et al.* Reducing the impact of Auger recombination in quasi-2D perovskite light-emitting diodes. *Nature Communications* **12**, 1–10 (2021).
13. Du, P. *et al.* Efficient and large-area all vacuum-deposited perovskite light-emitting diodes via spatial confinement. *Nature Communications* **12**, 4751 (2021).
14. Kioupakis, E., Rinke, P., Delaney, K. T. & Van de Walle, C. G. Indirect Auger recombination as a cause of efficiency droop in nitride light-emitting diodes. *Applied Physics Letters* **98**, 161107 (2011).
15. Liu, W. *et al.* Impact of defects on Auger recombination in c -plane InGaN/GaN single quantum well in the efficiency droop regime . *Applied Physics Letters* **116**, 222106 (2020).